Journal of Materials Research and Technology 42 (2026) 2041–2056

Contents lists available at ScienceDirect

Journal of Materials Research and Technology

journal homepage: www.elsevier.com/locate/jmrt

Improved corrosion resistance of a dual-phase Mg–Li–Al–Zn alloy via partial Zn substitution with Gd

Yi Chen [a], Lianmei Wu [b], Xiaolong Cui [c], Meng Fang [d], Gang Zeng [d], Jia Deng [a], Yonghao Gao [a,*], Fang Yi [e,**]

[a] School of Materials Science and Engineering, Central South University, Changsha, 410083, China
[b] Beijing Institute of Electronic System Engineering, Beijing, 100854, China
[c] Beijing Institute of Remote Sensing Equipment, Beijing, 100000, China
[d] Hunan Provincial Technology Innovation Center of New Light Alloy Materials for Aerospace, CASIC (Changsha) Advanced Materials Institute Co., Ltd, Changsha, 410205, China
[e] Xiangya School of Stomatology, Central South University, Changsha, 410008, Hunan, China

ARTICLE INFO

Keywords:
Mg–Li alloy
Microstructural characterization
Corrosion rate
TOF-SIMS

ABSTRACT

Zn was partially substituted with Gd in a dual-phase Mg–Li–Al–Zn (LAZ) alloy, aiming to further reduce the density of these ultra-light materials. The effects of Gd addition (LAZ-Gd) and subsequent annealing treatment (LAZ-Gd-T) on the microstructural evolution and corrosion behavior of the alloys were investigated. The Gd-containing alloys exhibited a lower density of 1.50 g cm^{-3} compared to the baseline LAZ alloy (1.52 g cm^{-3}). Microstructural analysis showed that the LAZ alloy consists of a β-Li + α-Mg dual-phase along with significant amounts of secondary (Al,Zn)Li and $(Li,Mg)_3(Al,Zn)$ phases. Partial substitution of Zn with Gd suppressed the formation of (Al,Zn)Li and $(Li,Mg)_3(Al,Zn)$ phases, while promoting the precipitation of the Al_2Gd intermetallics. Fine $(Li,Mg)_3(Al,Zn)$ and coarser (Al,Zn)Li phases re-precipitated in LAZ-Gd-T, which mitigated galvanic corrosion activity. The LAZ-Gd alloy developed a more protective corrosion film, attributed to a higher aluminum oxide content and a distribution of Gd oxides within the corrosion layer. Therefore, Gd alloying reduced the corrosion rate of the LAZ alloy from 2.55 mm/y to 0.63 mm/y (LAZ-Gd). Annealing slightly increased the corrosion rate to 1.29 mm/y in the LAZ-Gd-T condition. This work provides valuable insights into designing lighter Mg–Li based alloys with simultaneously enhanced corrosion resistance.

1. Introduction

Alloying magnesium with lithium is an effective approach to further reduce the weight of light alloys. The density of magnesium-lithium alloys typically falls within 1.35-1.65 g/cm^3, corresponding to about two-thirds to three-quarters that of conventional magnesium alloys, or one-half to two-thirds that of aluminium alloys [1–5], depending on the lithium content and other alloying additions. As a result, magnesium-lithium alloys are the lightest metallic structural materials currently available, offering high specific stiffness and excellent specific strength. Additionally, when the lithium content ranges between 5.7 and 10.3 *wt%*, the alloy exhibits a dual-phase microstructure consisting of α-Mg (hcp) and β-Li (bcc) phases. [1,6–8]. The coexistence of α-Mg phase and β-Li phase can result in excellent formability and plasticity [9]. These characteristics make them particularly attractive for applications where extreme weight reduction is critical [10].

However, the yield strength of conventional binary Mg–Li alloys in the deformed state is only about 80 MPa [11–13], it is necessary to introduce a third or fourth alloying element for strengthening. Al and Zn are ideal candidates for reinforcing the Mg–Li matrix. Both Al and Zn elements can strengthen Mg–Li alloys through both solid solution and second-phase precipitation. Specifically, when Al content exceeds 2 wt %, strengthening precipitates such as $MgLi_2Al$, AlLi, and $Mg_{17}Al_{12}$ are formed in the alloy, and their volume fraction and the resulting strengthening effects increase with increasing Al content [14,15]. Zn primarily contributes to solid solution strengthening, but at higher Zn contents, the MgLiZn and $MgLi_2Zn$ strengthening phase can also precipitate during aging treatment [11,14]. Therefore, many commercial

* Corresponding author.
** Corresponding author.
E-mail addresses: gaoyonghao_009@163.com (Y. Gao), yifangcsu@163.com (F. Yi).

https://doi.org/10.1016/j.jmrt.2026.03.205
Received 31 January 2026; Received in revised form 6 March 2026; Accepted 24 March 2026
Available online 25 March 2026

Mg–Li alloys containing Al and Zn had been developed, such as LA43 M, LA91 M, and LA103Z, as specified in GB/T 38063-2019. The yielding strength of these Mg–Li alloys have been effectively improved to around 120 MPa, significantly higher than that of binary Mg–Li alloys.

Nevertheless, the addition of the alloying elements, like Al and Zn, inevitably compromises the alloy's inherent advantage in lightweight performance. When the Zn content in the Mg–11Li binary alloy is increased to 3 *wt* % and 6 *wt* %, its density increases from the original 1.47 g/cm^3 to 1.52 g/cm^3 and 1.55 g/cm^3, respectively [11]. Recent studies have demonstrated that the addition of trace rare-earth elements (≤0.6 wt %) such as Y [16], Gd [17], and Ce [18] can enhance the mechanical properties of Mg–Li alloys by refining the grain structure and forming corresponding secondary phases. These rare-earth elements are expected to replace Al and Zn in Mg–Li alloys to achieve a balance between mechanical properties and density. Among them, Gd has attracted particular attention because of its high strengthening efficiency at trace addition levels and its strong interaction with Al, which facilitates the formation of stable Al–Gd intermetallic phases and effective grain refinement. To further reduce the density of LA103Z (Mg–10Li–3Al–3Zn), the content of the relatively heavy element Zn was decreased in this study, while a trace amount of Gd was introduced to compensate for the loss in its mechanical properties. The modified alloy has proven exhibiting improved mechanical properties and reduced density.

At present, numerous studies have been conducted to elucidate the effects of different alloying elements and heat treatments on the corrosion behavior of Mg–Li alloys. The strengthening secondary phases formed by the addition of Al and Zn act as cathodes, inducing galvanic corrosion and thereby deteriorating the corrosion resistance of Mg–Li alloys [19–21]. Rare-earth alloying can modify the secondary phases in Mg–Li–Al–Zn alloys into intermediate phases with smaller potential differences relative to the matrix, thereby enhancing their corrosion resistance [22,23]. It can be concluded that the effect of alloying on the corrosion behavior of Mg–Li alloys is mainly attributed to the secondary phases formed by alloying. Heat treatment can also regulate these secondary phases, thereby influencing the corrosion behavior of the alloy. In Mg–Li alloys, heat treatment may promote the partial dissolution of secondary phases into the β-Li matrix, including intermetallic compounds such as AlLi, $MgLi_2Zn$, and MgLiZn, as well as the α-Mg phase [24–26]. This process weakens micro-galvanic corrosion and consequently enhances the corrosion resistance and mechanical properties of the alloy. Therefore, heat treatment was also applied to the investigated alloy in the present study to clarify how thermally induced microstructural evolution influences corrosion behavior and to provide a scientific basis for optimizing processing parameters that balance mechanical performance and corrosion resistance. However, despite extensive research on the effects of individual alloying elements and heat treatment, studies investigating the combined influence of multi-element alloying and thermal processing on the corrosion behavior of Mg–Li alloys remain limited. The complex interactions among multiple alloying elements and their evolution during heat treatment are not yet fully understood, leaving the underlying mechanisms governing corrosion behavior in multi-component Mg–Li systems insufficiently clarified.

By partially substituting Zn with Gd and applying anneal treatment after forging, the mechanical properties of the high-lithium dual-phase Mg–Li–Al–Zn alloy were preserved. However, the effects of alloying and heat treatment on the corrosion behavior of this alloy remain unclear. In this study, a comparative analysis was conducted to evaluate the effects of Gd alloying and heat treatment on the microstructural characteristics and corrosion performance of a Mg–Li–Al–Zn-(Gd) alloy.

2. Materials and methods

2.1. Materials preparation and density test

Pure Mg (>99.99 wt %), pure Li (>99.9 wt %), pure Al (>99.99 wt %), pure Zn (>99.99 wt %), and Mg-30 wt % Gd master alloy were melted using a vacuum induction furnace at 730 °C under an argon atmosphere. The melts were then subjected to vertical DC casting to get ingots of Mg–Li–Al–Zn (hereafter designated as LAZ) and Mg–Li–Al–Zn-Gd (LAZ-Gd) with diameter of 240 mm and height of 500 mm. Samples with initial dimensions of 70 × 70 × 100 mm^3 were machined from the ingots for multidirectional forging. Both the samples and the dies were pre-heated to 300 °C prior to the process. After 9 forging passes, the final sample size was approximately 60 × 80 × 100 mm^3. The as-forged LAZ-Gd sample was subsequently annealed at 280 °C for 3 h and is designated as LAZ-Gd-T. The chemical composition of the alloys was determined using an inductively coupled plasma optical emission spectroscope (ICP-OES, Spectro Blue Sop, Germany), and the results are listed in Table 1.

The alloy density was measured in accordance with the GB/T 1423 guideline. The measurements were performed using the Archimedes method on an analytical balance (AB204-N, Mettler-Toledo, Switzerland) with a precision of 0.0001 g. The sample weights were recorded in air (W_1) and in distilled water (W_2). The density was subsequently calculated using the following equation:

$$\rho = \frac{W_1}{W_1 - W_2} \times \rho_{water} \quad (1)$$

Where ρ_{water} is the density of the distilled water.

2.2. Microstructure characterization

The microstructure of the investigated alloys was conducted using an OLYMPUS BX51 M metallographic optical microscope (OM), a scanning electron microscopy (SEM, Tescan Mira3, Czech) coupled with an energy dispersive spectroscopy (EDS), and a transmission electron microscope (TEM, JEM-F200X). Quantitative analysis of phase fractions and microstructural feature sizes was carried out based on SEM backscattered electron (BSE) images using ImageJ Pro software. Due to the inability of the EDS to detect lithium, time-of-flight secondary ion mass spectrometry (TOF-SIMS, PHI Nano TOF3) was employed to characterize both the lateral and in-depth lithium distribution in the alloys. The phase compositions of the alloys were characterized using a D/Max 2500 VB X-ray diffractometer (XRD) with the Cu Kα radiation. XRD measurement was conducted in the coupled θ-2θ mode using a step size of 0.02° and a constant scan rate of 4°/min.

Thin foils for TEM observation were prepared using electrolytic twin-jet polishing. The samples were mechanically ground to a thickness of approximately 40-50 μm, followed by twin-jet polishing in an electrolyte comprising 3 vol% perchloric acid and 1 vol% nitric acid in ethanol. The polishing process was carried out at a temperature of −35 °C under an applied voltage of 25 V until perforation occurred. The obtained foils were subsequently rinsed with ethanol and dried naturally before TEM examination. For TOF-SIMS analysis, two types of specimens were prepared. For surface elemental distribution analysis, bulk specimens were mechanically ground and subsequently polished to obtain a smooth, oxide-free surface. Immediately after polishing, the samples were transferred into the analysis chamber via a vacuum transfer system to

Table 1
Chemical composition of experimental alloys.

Alloy	Actual composition (wt %)				
	Li	Al	Zn	Gd	Mg
LAZ	10.0	3.1	2.8	–	*Bal.*
LAZ-Gd	9.8	3.0	0.3	0.15	*Bal.*

minimize surface oxidation and contamination. For three-dimensional elemental distribution analysis, the specimens were similarly ground and polished, then immersed in a 3 *wt%* NaCl solution for 15 min to generate a corrosion film of about 2 μm. The TOF-SIMS depth profiles were acquired while the sample surface was progressively etched using a Bi_3^{2+} primary ion beam (2 kV, 100 nA). Both etching and data acquisition were confined to a 100 μm × 100 μm area. A total etch time of 80 min was applied, which was sufficient to penetrate the entire corrosion film.

2.3. Electrochemical measurements

Prior to immersion testing, all specimens were sequentially ground using 400, 800, and 2000 grit SiC abrasive papers. The ground specimens were then ultrasonically cleaned in ethanol to remove surface debris and contaminants, followed by drying in warm air. Corrosion tests were conducted within 15 min after surface preparation to minimize the influence of surface oxidation. The electrochemical tests were conducted using a three-electrode system, with the alloy sample serving as the working electrode. A saturated silver chloride electrode (Ag/AgCl) was applied as the reference electrode, and a platinum electrode as the counter electrode. The electrolyte was a 3 wt % NaCl solution, and the experiments were carried out at a constant room temperature of 25 ± 1 °C. The tests were performed using a Donghua electrochemical workstation (DH7000C). Potentio-dynamic polarization (PDP) testing was conducted using a scan rate of 1 mV/s in the range of −400 ~ +400 mV (*vs.* OCP). The electrochemical impedance spectroscopy (EIS) tests were conducted in a frequency range of 10^5 Hz to 10^{-2} Hz with a perturbation amplitude of 5 mV around the stabilized OCP. The acquired EIS diagrams were fitted using the commercialized *Z*-View software. Prior to polarization and EIS test, the samples were conditioned at the open circuit potential (OCP) for 60 min to ascertain a stable potential.

2.4. Hydrogen evolution and weight loss measurement

The corrosion rate of the samples was determined by quantifying hydrogen evolution and weight loss during immersion in a 3 *wt%* NaCl solution. Hydrogen gas released in the corrosion process was collected and continuously monitored using a drainage method. The released hydrogen volume can be converted into a corrosion rate, CR in mm/y, based on the well-established fact that the evolution of 1 mol of hydrogen corresponds to the consumption of 1 mol of magnesium:

$$CR = K_H \times \frac{V_{H_2}}{A \times t \times \rho} \tag{2}$$

After immersion, the samples were rinsed using a chromic acid solution (100 g Cr_2O_3 + 500 g H_2O) to remove the corrosion products, thoroughly dried in a vacuum oven, and then reweighted to determine the weight loss. The corrosion rate *CR* in mm/y, was calculated based on the following equation [27]:

$$CR = K_W \times \frac{\Delta W}{A \times t \times \rho} \tag{3}$$

in the above Equations, $K_H = 93.85$ and $K_W = 8.76 \times 10^4$ are the unit conversion constants, V_{H_2} (ml) is the released hydrogen volume, ΔW (g) refers to the weight loss during immersion, A (cm^2) is the sample surface area exposed to the corrosive medium, t (h) is the immersion time and ρ (g/cm^3) is the density of the sample, determined using the Archimedes method.

3. Results and discussion

3.1. Metallographic characterization

Fig. 1 shows the microstructures of the studied alloys. The optical micrographs shown in Fig. 1(a–c) reveals numerous irregularly shaped embeds, along with smaller granular dark precipitates distributed within

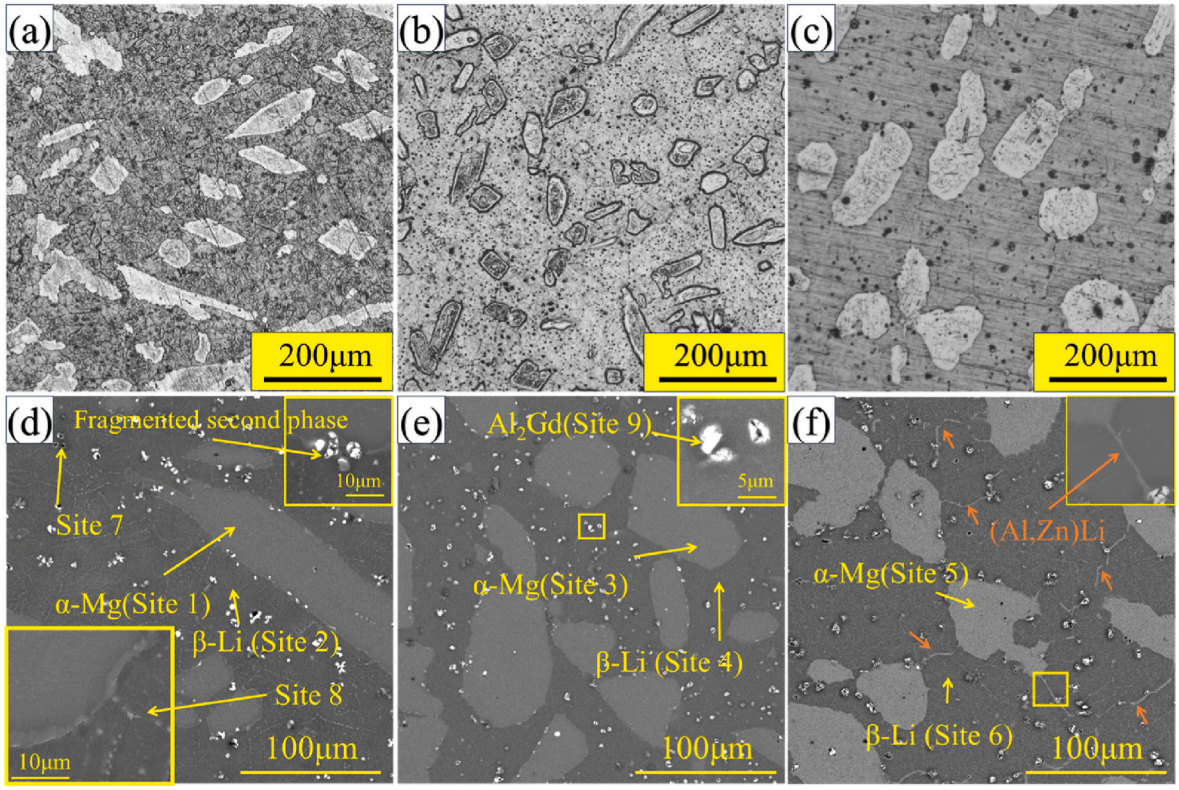

Fig. 1. (a-c)Optical micrographs and (d-f) SEM images of studied alloys: (a, d) LAZ, (b, e) LAZ-Gd and (c, f) LAZ-Gd-T alloy.

the matrix. The embeds (confirmed as α-Mg by the subsequent elemental distribution and phase composition analyses) exhibited different geometrical characteristics in the three alloys. For example, the average size of the embeds differed among the alloys, decreasing from 24.19 μm in the LAZ alloy to 18.37 μm in the LAZ-Gd alloy. Following annealing, the embeds in the LAZ-Gd-T alloy exhibited significant coarsening, reaching an average size of 22.95 μm. However, the volume fraction of the embeds was not altered by substituting Zn with Gd; it was measured to be approximately 26.4% in both the LAZ and LAZ-Gd alloys. The subsequent annealing treatment, however reduced their volume fraction to 24.9% in the LAZ-Gd-T alloy. Differences in the volume fractions of the secondary phases were also observed among the studied alloys. Specifically, a volume fraction of approximately 2.1% was identified in the LAZ alloy, which decreased to 1.63% in the LAZ-Gd alloy, likely due to the lower overall alloying concentration (Table 1). The annealing treatment only slightly reduced the volume fraction of the secondary phases, possibly because the annealing temperature was not sufficiently high to promote their dissolution. It should be noted that the phase fractions were quantified based on SEM micrographs, which primarily capture microscale features and may not fully resolve nanoscale precipitates; therefore, the reported values mainly reflect the distribution of coarse second phases.

The morphologies of the studied alloys were also investigated using SEM in backscattered electron (BSE) imaging mode, with the results presented in Fig. 1(d–f). The granular dark precipitates visible in the optical micrographs appear as bright contrasts in the BSE images, suggesting the enrichment of heavier elements. In the LAZ alloy, the precipitates are mostly randomly distributed, although some tend to form preferentially along the grain boundaries. The precipitates formed at the grain boundaries are markedly finer than those observed along the α-Mg/β-Li interphase interfaces. Interestingly, partial substitution of Zn with Gd altered the distribution of the secondary phases, as no preferential precipitation along the grain boundaries was observed in the LAZ-Gd alloy. During the subsequent annealing treatment, partial dissolution of the secondary precipitates occurred, resulting in fewer bright particles in the LAZ-Gd-T alloy and a correspondingly less pronounced contrast in the BSE images. Meanwhile, quasi-continuous precipitates were also formed along the grain boundaries of β-Li phases, as indicated by the orange arrows in Fig. 1(f).

The chemical compositions of those distinct features (as labeled using numbers in Fig. 1) observed in the BSE images were quantified using EDS, and the results are summarized in Table 2. It is worth noting that lithium is not included in Table 2, which does not imply its absence in the detected regions, but rather reflects the limitation of EDS, which can only detect elements with atomic numbers $Z > 3$. The aforementioned embeds in the LAZ alloy (Site 1#) are predominantly composed of Mg, with smaller amounts of Al (2.8 *wt%*) and Zn (1.7 *wt%*). After partially substituting Zn with Gd, the chemical composition of the embeds in the LAZ-Gd alloy includes Al, Zn, and Gd, differing from that of the LAZ alloy. Moreover, the relative Al concentration increases markedly to 3.5 *wt%* in the embeds (Site 3#) of LAZ-Gd alloy, primarily due to the reduced content of the heavier element Zn (0.1 *wt%*). The Gd content in the embeds of the LAZ-Gd alloy is also slightly higher than the nominal bulk Gd addition. The concentrations of Al, Zn, and Gd in the embeds further evolve after annealing. Specifically, in the LAZ-Gd-T alloy, Al and Zn become more enriched in the embeds, likely as a result of solid-solution effects induced by annealing at elevated temperature.

The elemental compositions of the matrix (Sites 2#, 4#, and 6#) were also characterized. The Al content in the matrix of each alloy is significantly lower than that in the embeds, whereas the Zn concentration is comparatively higher. In the LAZ alloy, the Zn content in the matrix is noticeably higher than the nominal bulk addition, indicating that Zn prefers to remain in solid solution within the matrix rather than partitioning into the embeds. In contrast, the matrix of the LAZ-Gd alloy contains approximately the same amount of Zn as the nominal addition; however, additional Zn becomes dissolved in the matrix after annealing. Although the absence of Li detection may affect quantitative accuracy, the compositional trend inferred here is validated by subsequent analysis. Concentrated alloying elements were detected in the granular secondary precipitates (Sites 7#, 8#, and 9#). In the LAZ alloy, the relative concentration of Zn compared with Al in the isolated secondary particles (Site 7#) is noticeably lower than that in the particles distributed along the grain boundaries (Site 8#). Nevertheless, Zn was not detected in the secondary precipitates of the LAZ-Gd alloys, where only concentrated Al and Gd were observed at Site 9#. This observation is reasonable, as it is well established that Al preferentially combines with rare-earth elements-Gd in the present case-to form intermetallic compounds. The atomic ratio of Al to Gd is approximately 2.5, which is close to the stoichiometric ratio of the commonly reported Al_2Gd phase. Therefore, the presence of Al_2Gd can be reasonably inferred. This phenomenon is similar to that observed in Mg-(Li)–Al alloys containing rare-earth elements such as Y,Ce and La, where Al_2RE precipitates are formed [22,23,28,29]. The quasi-continuous phases observed in the LAZ-Gd-T alloy are composed primarily of Al and Zn, and may also contain Li, which cannot be detected by EDS. Although Mg was detected at all examined sites, a quantitative comparison was not conducted because the EDS measurement unavoidably collects signals from a broader region than the precise point of interest, which could compromise the accuracy of the Mg quantification.

To overcome this limitation, time-of-flight secondary ion mass spectrometry (TOF-SIMS) was employed to analyze the LAZ-Gd sample. Fig. 2 presents the elemental distribution maps, including that of lithium. The results indicate that the Mg-rich circular regions correspond to the α-Mg phase embedded within the β-Li matrix. It can be observed that the Li-depleted regions in the Li map are smaller in area than the Mg-enriched regions in the corresponding Mg map, suggesting elemental segregation between the α-Mg and β-Li phases. Aluminum is primarily dissolved in the α-Mg phase, whereas zinc exists as a solid solution within the β-Li phase. These elemental distribution characteristics are in good agreement with the compositional trends obtained from the previous EDS analysis, confirming the preferential partitioning of Al and Zn between the α-Mg and β-Li phases. The Gd signal exhibits relatively low intensity, which is attributed to its predominant presence as Al_2Gd precipitates, accounting for only 0.22% of the total composition of the LAZ-Gd alloy.

3.2. Phase analysis by XRD

The phase constituents of the studied alloys were identified using XRD, and the corresponding diffraction patterns are shown in Fig. 3. In all three alloys, clear and intense diffraction peaks corresponding to the

Table 2
EDS results collected from the points marked in Fig. 1.

Element	Elemental Concentration (*wt.%*)								
	1	2	3	4	5	6	7	8	9
Mg	95.5	94	96.2	98.2	94.9	96.5	35.7	89.3	27.8
Al	2.8	1.4	3.5	1.4	4.7	2.8	38.1	5.3	21.4
Zn	1.7	4.6	0.1	0.3	0.3	0.4	26.2	5.4	–
Gd	–	–	0.2	0.1	0.1	0.3	–	–	50.8

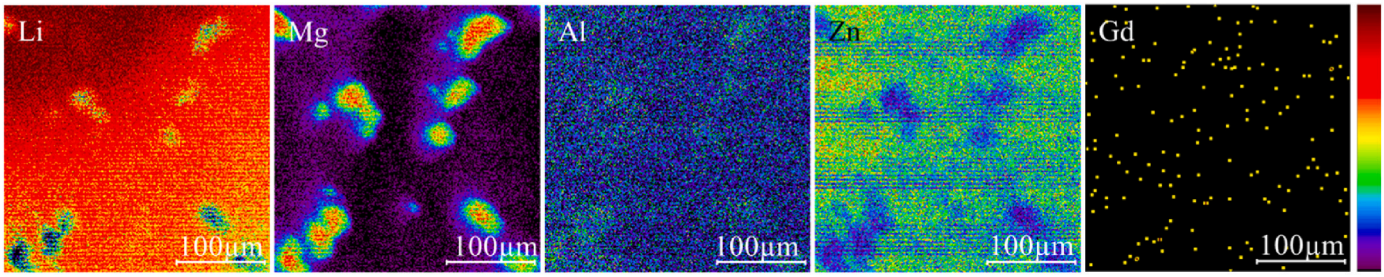

Fig. 2. Elemental distribution of the LAZ-Gd alloy derived using TOF-SIMS.

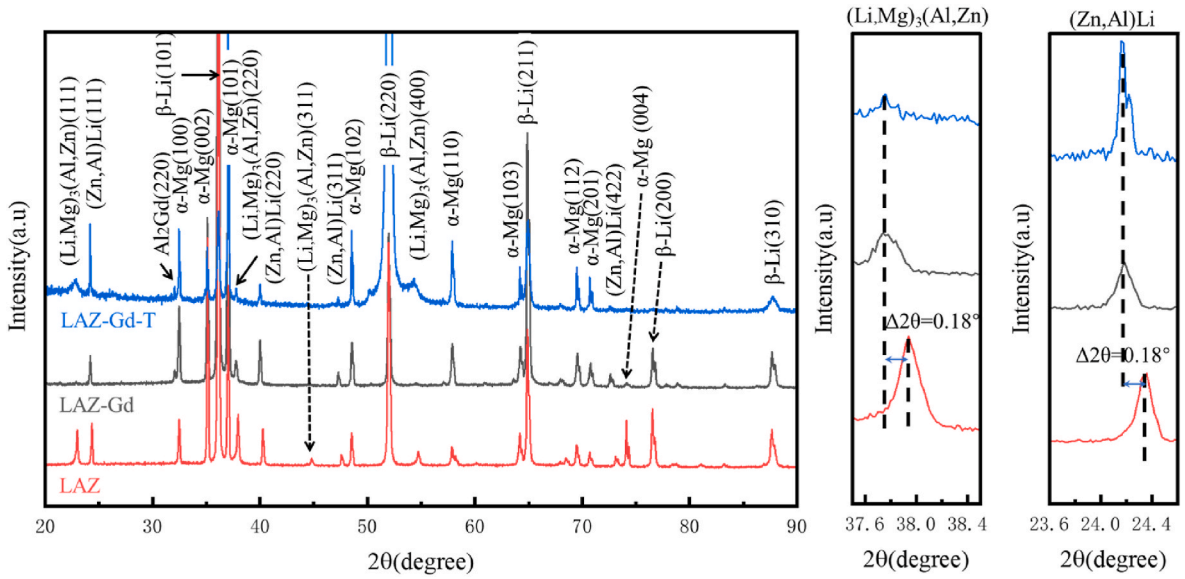

Fig. 3. XRD patterns of LAZ alloy, LAZ-Gd alloy and LAZ-Gd-T alloy.

α-Mg and β-Li phases were observed, indicating that each alloy exhibits a dual-phase structure. Combined with the elemental distribution analysis, it is evident that the matrix and the embeds observed in Fig. 1 correspond to the β-Li and α-Mg phases, respectively. This $\alpha + \beta$ dual-phase structure is consistent with the alloy compositions, which lie precisely within the two-phase region of the Mg–Li binary phase diagram.

Apart from the dominant α and β phases, additional secondary phases were also identified in the alloys. In particular, distinct diffraction peaks were observed at $2\theta = 22.9°$, 37.9°, 44.7°, 54.68°, matching the standard diffraction pattern of Li_2MgAl (*Fd-3m*, $a = 0.67$ nm, PDF #03-065-5657) with a cubic crystal structure. The good agreement in both peak position and relative intensity indicates that the secondary phase retains a Li_2MgAl-type crystal framework. EDS analysis of these precipitates (Table 2) reveals the presence of Zn in addition to Mg, and Al, indicating a deviation from the ideal Li_2MgAl stoichiometry. Such simultaneous substitution within both cation sublattices has been predicted in Mg–Li–Al–Zn alloys by combining TEM characterization with first-principles calculations [30]. Therefore, the secondary phase in the present study is described as a Li_2MgAl-type phase with partial elemental substitution, denoted as $(Li,Mg)_3(Al,Zn)$ to reflect its compositional variation. However, EDS analysis indicates that the secondary phases contain a considerable amount of Zn (Table 2). Therefore, these peaks are indexed as $(Li,Mg)_3(Al,Zn)$ in Fig. 3, consistent with the results reported in Ref. [30]. The $(Li,Mg)_3(Al,Zn)$ phase can be regarded as a Zn-containing variant of Li_2MgAl.

Moreover, additional phase resulting diffraction peaks at approximately $2\theta = 24.4°$, 40.3°, 47.6° and 73.2° were also detected in all the alloys. This phase exhibits the same crystallographic structure as the standard AlLi phase (*Fd-3m*, $a = 0.637$ nm, PDF #00-003-1215), despite its more complex chemical composition revealed by the EDS analysis. Following the interpretation in Ref. [31], this phase is designated as (Al, Zn)Li in the present study. However, the incorporation of Zn into the AlLi-type compounds altered the lattice parameters and consequently shifted the corresponding diffraction peak positions. For example, in the LAZ alloy, the diffraction peaks corresponding to the (Al,Zn)Li phase shifted toward higher 2θ values compared with those of the standard AlLi phase, indicating a reduction in interplanar spacing.

By substituting Zn with Gd, the primary phase compositions remained unchanged, although the interplanar spacings of the secondary phases were affected. As shown in the magnified view of the diffraction peaks, those associated with the $(Li, Mg)_3(Al, Zn)$ and (Al,Zn) Li phases in the LAZ-Gd and LAZ-Gd-T alloys had shifted by approximately 0.18° toward lower 2θ values relative to the LAZ alloy, indicating increased interplanar spacing and lattice expansion. This shift may be attributed to the reduced Zn content in the LAZ-Gd alloy compared with the LAZ alloy, resulting in compositional variation within the $(Li, Mg)_3(Al,Zn)$ phase. An increase in the Al/Zn ratio may lead to an expansion of the lattice parameters, since the atomic radius of Al (0.143 nm) is slightly larger than that of Zn (0.133 nm). The increased Al fraction expands the lattice spacing of the $(Li,Mg)_3(Al,Zn)$ phase, resulting in a lower-angle peak shift. The identification of the Al_2Gd phase in the LAZ-Gd alloy, as evidenced by the diffraction peak at $2\theta = 32.03°$, confirms the formation of Gd-containing intermetallic compounds(in Fig. 1 (e)). It has been widely reported that Al readily reacts with rare-earth (RE) elements to form Al_2RE compounds [22,23]. Indeed, the EDS spectrum collected from Site #9 in Fig. 1 indicates an Al:Gd atomic ratio of approximately 2.4, which is reasonably close to the

stoichiometric ratio of 2,with the deviation likely arising from the semi-quantitative nature of the EDS technique.

3.3. Microstructure characterization by TEM

To further investigate the effects of alloying and heat treatment on the as-forged LAZ alloys, TEM characterization was also conducted on the studied alloys, and the results are displayed in Figs. 4 and 5. Fig. 4(a) presents the bright-field image obtained from the LAZ-Gd-T alloy, and several secondary-phase particles had been identified. The SAED pattern obtained from the captured particles (with a diameter of approximately 1 μm) confirmed that they possess a cubic crystal structure, with a calculated lattice constant of 0.6 nm. This value is very close to that of the AlLi phase (0.63 nm [32]). Considering their identical crystal structure, the particles were therefore identified as (Al,Zn)Li. The incorporation of Zn into the crystal structure was confirmed by EDS analysis in Table 2.

In the bright-field image of the LAZ-Gd alloy, several types of secondary particles were observed. These include sparse, small spherical particles (as marked with the red arrows in Fig. 4(c))with an average equivalent diameter of approximately 297 ± 89 nm; two much larger particles (marked with a yellow circle in Fig. 4(c)) with diameters of about 3.45 ± 0.17 μm; and the purple triangles in Fig. 4(c) emphasize the slim, elongated secondary particles (likely composed of multiple tiny, spatially indistinguishable particles). The SAED pattern obtained from the larger particles, with the zone axis parallel to the [611] crystallographic direction, is shown in Fig. 4(d). This pattern confirms a cubic crystal structure. The lattice constant was calculated to be a = 0.73 nm, which is in good agreement with the reported value for the Al_2Gd phase (a = 0.79 nm) [25]. Therefore, the selected secondary particle was identified as Al_2Gd, consistent with the XRD analysis shown in Fig. 3.

The crystal structure of the spherical secondary particles identified in Fig. 4(c) was also examined using high-resolution TEM (HRTEM) and the corresponding FFT pattern with the results presented in Fig. 5(b and c). EDS mapping indicated that these particles are primarily composed of Mg, Al, Zn and possibly EDS indetectable Li. The interplanar spacings of the (0-22) crystallographic planes measured from different particles were 2.62 Å (Fig. 5 (b)) and 2.35 Å (Fig. 5 (c)), corresponding to a lattice constant of 7.41 Å and 6.64 Å, respectively. Although these values exhibit some scatter, they fall precisely within the range reported for the $(Li,Mg)_3(Zn/Al)$ phase in Ref. [30], suggesting that these secondary particles are indeed $(Mg,Li)_3(Al,Zn)$. The scattered lattice constant calculated may be attributed to their varying chemical compositions, which had also been reflected in by the shifting XRD peak positions shown in Fig. 3. The lengthy particles observed in Fig. 4(c) was also characterized using HRTEM as shown in (Fig. 5 (d). The results confirm that these particles share the same crystal structure and phase composition, $(Mg,Li)_3(Al,Zn)$, as the spherical particles. Similar secondary phase composition had also been demonstrated in the LAZ alloy, as shown in Fig. 5 (a).

3.4. Electrochemical corrosion evaluation

The open circuit potential (OCP) evolution curves of the LAZ, LAZ-Gd, and LAZ-Gd-T alloys in 3 wt% NaCl solution are presented in Fig. 6. For all alloys, the OCP exhibits a rapid positive shift during the initial immersion stage, indicating the fast formation of surface corrosion products. After approximately 500-800 s, the potential variation becomes significantly slower and gradually approaches a quasi-steady state with only minor fluctuations. Among the three alloys, the LAZ-Gd-T alloy maintains the most positive OCP over the entire immersion period, followed by LAZ-Gd, while the LAZ alloy shows the lowest potential. Although a slight positive drift is still observed at longer immersion times, the variation rate is small, suggesting that a dynamic equilibrium between film formation and dissolution has been established. The polarization measurements were carried out after the OCP reached this quasi-stable condition to ensure reliable electrochemical evaluation.

Fig. 7 presents the potentiodynamic polarization curves of the studied alloys in a 3 *wt%* NaCl solution. It is evident that during anodic polarization, the current density increased sharply with only a small overpotential, indicating that the samples did not exhibit any passivation behavior. The cathodic branches of all samples display very similar trends, suggesting that the same cathodic reactions occurred in each alloy. The polarization curves were analyzed using the Tafel extrapolation method. In the present study, the commonly accepted criteria were applied to determine the linear Tafel region: the overpotential must exceed 50 mV, and the linear segment must extend over at least one decade on the current density axis. According to these criteria, clear Tafel linear regions were identified on the cathodic branches, whereas no reliable Tafel region was observed on the anodic branches. In this case, the exact corrosion current density (i_{corr}) was derived based on Tafel extrapolating the cathodic branches.

The values of corrosion potential (E_{corr}), corrosion current density (i_{corr}), and cathodic Tafel slope (β_c) are listed in Table 3. Although all the samples exhibit nearly identical corrosion potentials of approximately −1.55 V *vs.* Ag/AgCl, their corrosion current densities differ significantly. A corrosion current density of 140 μA/cm^2 was derived from the LAZ alloy. After substituting Zn with Gd, the corrosion rate of the sample had been dramatically reduced, yielding an i_{corr} value of 50 μA/cm^2 for the LAZ-Gd alloy. The corrosion rate was slightly reduced to 44 μA/cm^2 for the LAZ-Gd-T alloy. The reduced corrosion current density might be attributed to the much lower volume fraction of the secondary phases in the LAZ-Gd alloy, as analyzed in Fig. 1. It has been well accepted that the secondary phase particles are electrochemically nobler than the surrounding matrix, promoting galvanic corrosion.

The corrosion performance of the studied alloys was also comparatively investigated using EIS technique, the resulting Nyquist plots are presented in Fig. 8. Three loops can be identified from the Nyquist plot of the LAZ alloy: two distinguishable capacitive loops in the high-to-medium frequency range and one inductive loop in the fourth quadrant, characterized by its positive imaginary impedance, spanning the low-frequency range. The capacitive loop at high frequency is

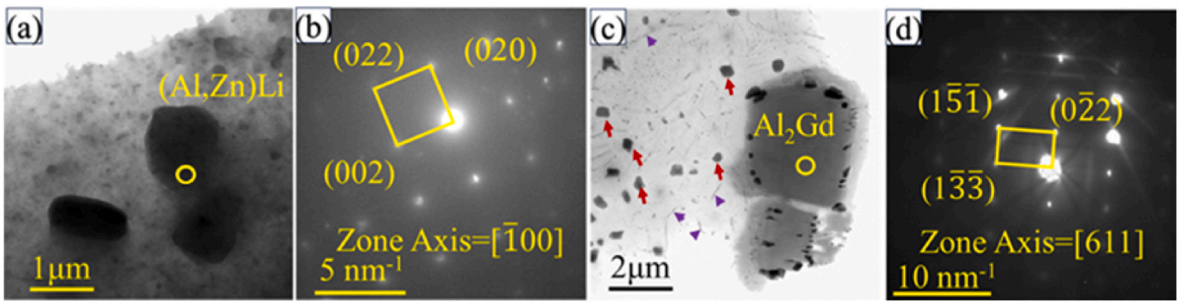

Fig. 4. (a,c) Bright-field TEMimages and (b,d) corresponding SAED patterns of the secondary phases: (a,b) (Al,Zn)Li in LAZ-Gd-T, (c,d) Al_2Gd in the LAZ-Gd alloy.

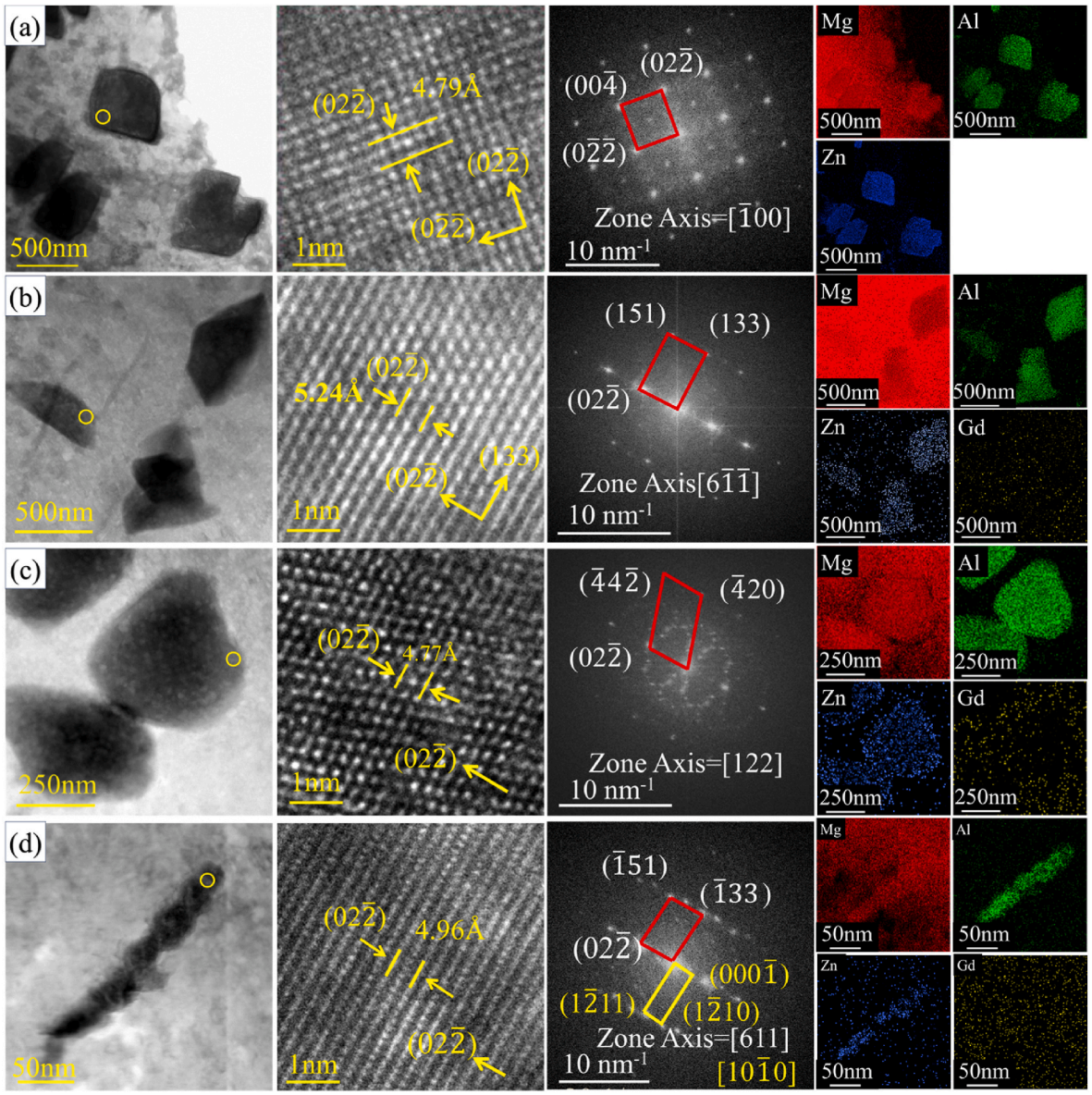

Fig. 5. Bright-field (BF) images, high-resolution TEM (HRTEM) images, FFT spectrum, and elemental distribution maps of the $(Li,Mg)_3(Al,Zn)$ phase from (a) LAZ and (b-d) LAZ-Gd alloy.

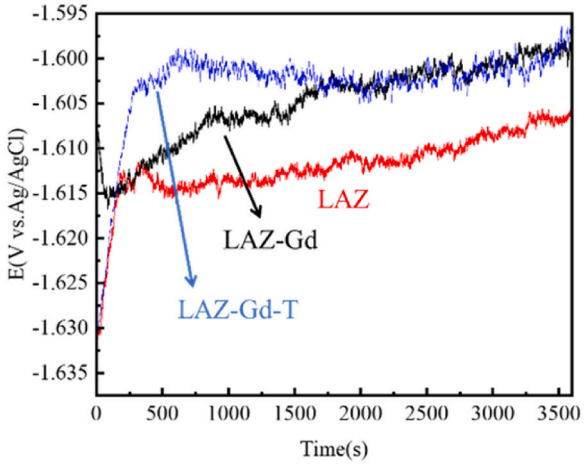

Fig. 6. Open circuit potential (OCP) evolution of LAZ, LAZ-Gd and LAZ-Gd-T alloys in 3 wt% NaCl solution.

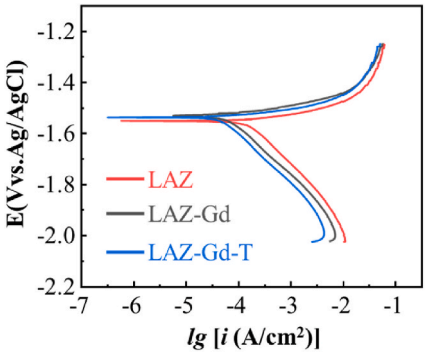

Fig. 7. Potentiodynamic polarization plots of the studied alloys in 3 wt % NaCl solution.

significantly smaller compared to that in the medium frequency range. Partial substitution of Zn with Gd resulted in the disappearance of the

Table 3
Tafel fitting results of the three alloys.

Alloy	E_{corr} (V *vs* Ag/AgCl)	i_{corr} (μA/cm^2)	β_c (mV/decade)
LAZ	−1.55	140	−196
LAZ-Gd	−1.53	50	−182
LAZ-Gd-T	−1.55	44	−192

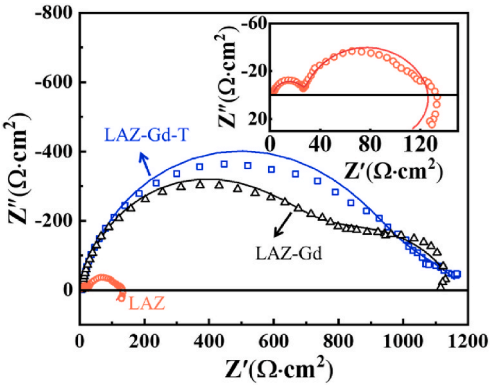

Fig. 8. EIS Nyquist plots of the studied alloys in a 3 wt % NaCl solution. The solid lines represent the fitting results, while the scattered symbols display the experimental data.

inductive loop on the Nyquist plot of the LAZ-Gd alloy, and the relative diameters of the two capacitive loops were altered. Specifically, the high-frequency loop expanded considerably, becoming much larger than the medium-frequency loop. Additionally, the overall size of the Nyquist plot for the LAZ-Gd alloy is much larger than that of the LAZ alloy, indicating improved corrosion resistance. After the subsequent annealing treatment, the Nyquist plot of the LAZ-Gd-T alloy displayed two indistinguishable capacitive loops, with its overall size slightly enlarged compared to that of the LAZ-Gd alloy, suggesting the best corrosion resistance of the LAZ-Gd-T alloy.

The changes in the geometrical characteristics of the Nyquist plots reflect alterations in the corrosion process of the studied alloy. To investigate these changes, the corresponding Nyquist plots were analyzed using the equivalent circuit fitting technique. It has been well reported that the high-frequency capacitive behavior arises from the charge transfer process, while the medium-frequency capacitive behavior is due to the ineffective protection behavior of the corrosion film accumulation on the sample surface [33]. The inductive loop is attributed to the slower processes involved in corrosion, such as the adsorption and desorption of the corrosion by-products on the sample surface [34]. Because the Nyquist plot of the LAZ alloy exhibits two capacitive loops in the high- and medium-frequency regions together with an additional inductive response at low frequency, an equivalent circuit incorporating two capacitive elements and one inductive element was adopted to adequately describe its impedance behavior, as shown in Fig. 9 (a). After alloying, the inductive response disappears in the Nyquist plots of the LAZ-Gd and LAZ-Gd-T alloys, indicating a more stable corrosion process; therefore, a simplified equivalent circuit without an inductive element, as shown in Fig. 9 (b), was employed to fit their EIS data. In the circuits, R_s represents the resistance of the solution between the reference and working electrodes, R_t and CPE_t, in parallel connection, model the resistive and capacitive behavior of the charge transfer process [35], respectively. R_f and CPE_f, connected in parallel, accounts for the resistive and capacitive behavior of the corrosion film accumulated on the sample surface [36]. As explained, the series connection of R_L and L is included in the circuit to analogy the inductive behavior. The constant phase element (CPE) is utilized, instead of pure capacitor (C), in the proposed circuit because of the surface heterogeneity of the studied sample [37], largely due to the localized corrosion attack.

The experimental EIS diagrams were fitted against the proposed equivalent circuits, and the fitting parameters are listed in Table 4. All the three diagrams had been adequately fitted, with the corresponding Chi-square (χ^2) being less than 0.01. Obviously, after Gd alloying, the charge transfer resistance (R_t) dramatically increased from 25.6 Ω cm^2 (LAZ) to 729.0 Ω cm^2 (LAZ-Gd alloy), suggesting that Gd substitution significantly improve the intrinsic corrosion resistance of the matrix, possibly due to the apparently reduced secondary phase particles because of the reduced overall alloying element concentrations in the LAZ-Gd alloy (Table 1). R_t value further increased to 947.1 Ω cm^2 for the LAZ-Gd-T alloy, possibly because of the partial dissolution of the secondary phases and also the reduced volume fraction of the α-Mg embeds in the annealing process of the LAZ-Gd alloy, as observed in Fig. 1.

Additionally, the impedance associated with the corrosion film on the sample surface varied among the samples. The LAZ alloy exhibited the lowest R_f value of 99.3 Ω cm^2, while Gd substitution significantly increased the R_f value to 428.9 Ω cm^2 for the LAZ-Gd alloy. After annealing, the R_f value decreased to 233.3 Ω cm^2 for the LAZ-Gd-T sample. It has been reported that the R_f value indirectly reflects the porosity of the films, with higher R_f typically indicating finer pores in the corrosion film [38]. In this regard, more compact corrosion film might have been accumulated on the Gd-containing LAZ alloy. The capacitance of the corrosion film is directly related to the CPE_f-T value. In the present study, the CPE_f-T values for all the alloys are of the same order of magnitude, with the LAZ alloy showing a slightly higher value (2.3×10^{-4} Ω cm^{-2}·s^n) than the LAZ-Gd alloy (1.60×10^{-4} Ω cm^{-2}·s^n), and a marginally lower value than the LAZ-Gd-T alloy (4.0×10^{-4} Ω cm^{-2}·s^n). By comparing the R_f and CPE_f-T values, it can be inferred that the corrosion film formed on the Gd-containing alloy provides better corrosion protection than that on the LAZ alloy in line with similar reported findings [39].The inductive loop appears only in the Nyquist plot of the LAZ alloy, indicating that the addition of Gd has improved the uniformity of corrosion on the sample surface. However, this does not necessarily prevent the occurrence of localized pitting. The corrosion resistance of the samples can be evaluated by the difference between the impedance difference at zero frequency and infinity frequency [40]:

$$R_p = |Z|_{f\to 0} - |Z|_{f\to \infty} \quad (4)$$

According to Equation (4), the R_p values calculated for the LAZ, LAZ-Gd and LAZ-Gd-T alloys are, 101.1 Ω cm^2, 1217.2 Ω cm^2 and 1088.9 Ω cm^2, respectively. Therefore, the Gd-free alloy exhibit the worst

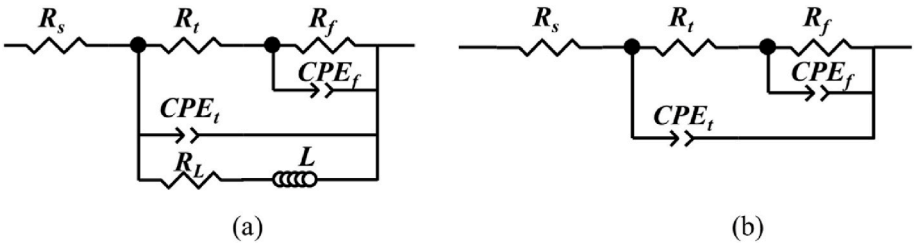

Fig. 9. Equivalent circuits used to analyze the EIS diagrams of (a) LAZ alloy and (b) LAZ-Gd and LAZ-Gd-T alloys after 60 min of exposure to 3 *wt%* NaCl.

Table 4
The fitting parameters used for the EIS analysis

Alloys	R_s /Ω·cm^2	R_t/Ω·cm^2	CPE_t-T/Ω·cm^{-2}·s^n	n_t	R_f /Ω·cm^2	CPE_f-T/Ω·cm^{-2}·s^n	n_f	R_L/Ω·cm^2	L/H·cm^2	χ^2
LAZ	2.4	25.6	2.7×10^{-6}	0.93	99.3	2.3×10^{-4}	0.85	92.0	1096	0.006
LAZ-Gd	5.5	729.0	3.3×10^{-5}	0.89	428.9	1.6×10^{-4}	0.69	/	/	0.003
LAZ-Gd-T	6.0	947.1	3.8×10^{-5}	0.88	233.3	4.0×10^{-4}	0.59	/	/	0.005

corrosion resistance, and the two Gd-containing alloys exhibited rather close overall corrosion resistance, which is consistent with the polarization evaluation (Table 3).

Both the PDP and EIS results indicate that Gd addition improves the corrosion resistance. However, the magnitude of the improvement differs markedly between the two methods: the PDP data suggest an increase of more than twofold, whereas the EIS analysis indicates a substantially higher enhancement of over one order of magnitude. This discrepancy can be attributed to the fact that the corrosion current density derived from Tafel extrapolation in PDP is typically interpreted under a simplified, charge-transfer-controlled assumption and does not explicitly account for mass-transport resistance. In contrast, EIS reflects the overall electrochemical impedance arising from both charge-transfer and mass-transport processes. Consistently, the medium-frequency Nyquist loop suggests that the charge-transfer resistance makes a non-negligible contribution.

3.5. Hydrogen evolution and mass loss measurements

Although the analysis of polarization curves and impedance spectra can provide insights into the corrosion behavior of the samples, accurately estimating the corrosion rate remains challenging. This is due to the assumption of uniform corrosion, which contrasts with the actual situation where localized pitting typically dominates the corrosion process of magnesium. Immersion tests were performed to evaluate the corrosion rate of the studied alloys, during which the hydrogen gas released was continuously monitored. The volume evolution of the H_2, during the immersion process for 7 days in the 3 *wt%* NaCl solution, are comparatively displayed in Fig. 10. It is evident that significantly more hydrogen was released from the LAZ alloy compared to the LAZ-Gd and LAZ-Gd-T alloys. Furthermore, the hydrogen volumes collected from the LAZ-Gd and LAZ-Gd-T alloys were quite similar, although the volume from the LAZ-Gd-T alloy was slightly higher than that from the LAZ-Gd alloy. The overall H_2 volume had been converted into the corrosion rate P_H in mm/y using Equation (2), and the calculation results are listed in Table 5. The P_H values of 2.58 mm/y, 0.77 mm/y and 0.92 mm/y had been derived from the LAZ, LAZ-Gd and LAZ-Gd-T alloys, respectively. Therefore, the LAZ alloy experienced the most severe corrosion during the immersion process, while the LAZ-Gd alloy exhibited the least

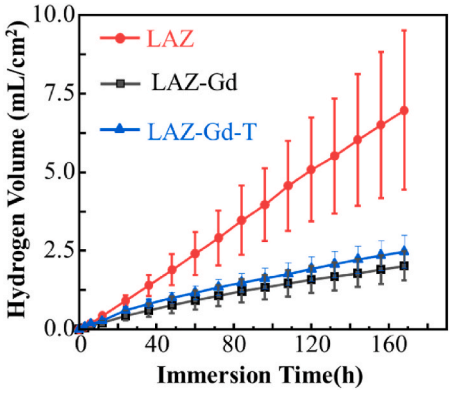

Fig. 10. Hydrogen evolution of the studied alloys during immersion in 3 wt % NaCl solution.

Table 5
Corrosion rates evaluated from hydrogen evolution and weight loss.

Alloy	ρ (g/cm^3)	V_H (7-day) (mL·cm^{-2}·day^{-1})	P_H (mm/y)	ΔW (mg·cm^{-2}·day^{-1})	P_W (mm/y)
LAZ	1.52	0.99	2.58	1.06	2.55
LAZ-Gd	1.50	0.29	0.77	0.26	0.63
LAZ-Gd-T	1.50	0.35	0.92	0.53	1.29

corrosion degradation. This corrosion trend aligns well with the expected results based on the calculated corrosion resistance, as derived from Equation (3). Moreover, all the H_2 evolution curves increased almost linearly with immersion time, although the slopes varied among the different samples. This linear increase suggests that corrosion propagates freely in both lateral and depth directions, and consequently, the corrosion products accumulated on the sample surface do not provide effective inhibition of the corrosion process.

During the immersion process, the samples underwent corrosion, resulting in a measurable mass change. The corrosion rate (P_w in mm/y) was calculated based on the mass change in the immersion process based on Equation (3), and the corresponding results are listed in the last column of Table 5. P_w values of 2.55, 0.63 and 1.29 mm/y, respectively were obtained for the LAZ, LAZ-Gd and LAZ-Gd-T alloys. As consistent with that evaluated from the hydrogen collection method, the LAZ alloy provided the highest corrosion rate. However, the immersion test results were inconsistent with the polarization curves, which had identified the LAZ-Gd alloy, rather than the LAZ-Gd-T alloy, as having the best corrosion performance. The discrepancy between corrosion rankings derived from PDP and immersion tests may stem from the different corrosion stages probed by these methods. PDP measurements mainly capture early-stage corrosion dominated by micro-galvanic effects, whereas in the long-term immersion test, the contribution of the surface film to the corrosion resistance became dramatic. Therefore, better protection of the corrosion film formed on the LAZ-Gd alloy can be inferred.

3.6. Corrosion morphology characterization

Fig. 11 shows the optical corrosion morphology of the studied alloys after varying immersion times in a 3 *wt%* NaCl solution for a maximum of 9 days. It is evident that after 3 h of immersion, all the sample surfaces were partially corroded, with only a small fraction of the initial surface remaining. The corroded areas exhibited typical uniform corrosion characteristics, likely resulting from the coalescence of the numerous localized, small pitting attacks.

It is evident that after 3 h of immersion, all the sample surfaces were partially corroded, with only a small fraction of the initial surface remaining. The corroded areas featured typical uniform corrosion characteristics, which could actually be the results of numerous localized tiny pitting attacks. The edges of the uncorroded regions on the LAZ alloy after 3 h' immersion has been highlighted using dashed red lines (as shown in Fig. 11). As for the two Gd-containing alloys, the uncorroded areas are discretely, other than continuously, distributed across the sample surface. Minimal changes in surface morphology were

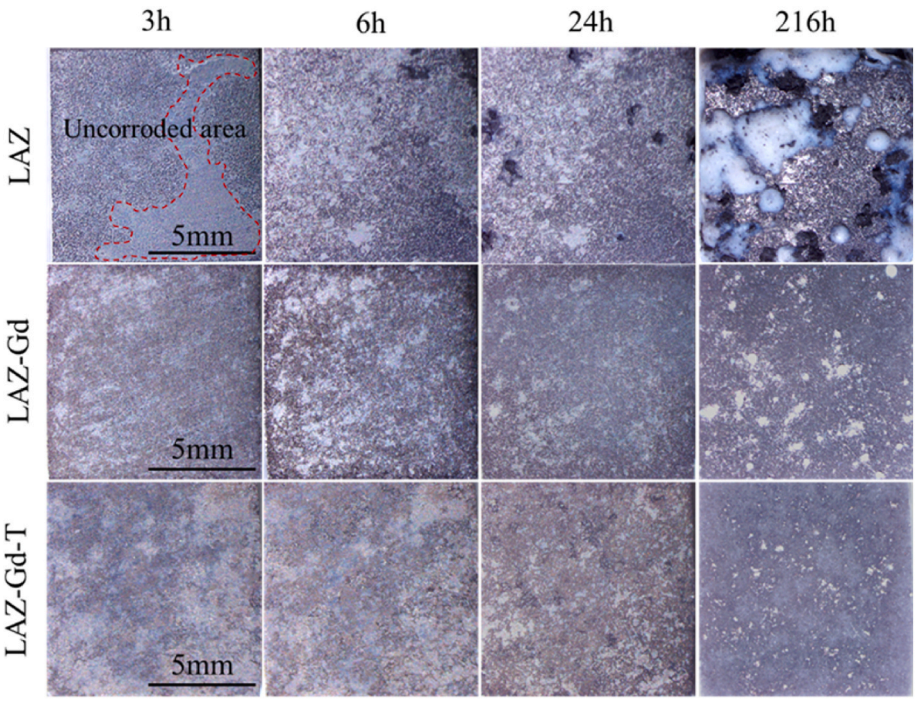

Fig. 11. Optical morphologies of the studied alloys after immersion for varying times.

observed for both the LAZ-Gd and LAZ-Gd-T alloys, even after the immersion time was increased to 216 h. In contrast, the corrosion morphology of the LAZ alloy was significantly affected by immersion time. After 6 h, the continuity of the uncorroded areas was disrupted,

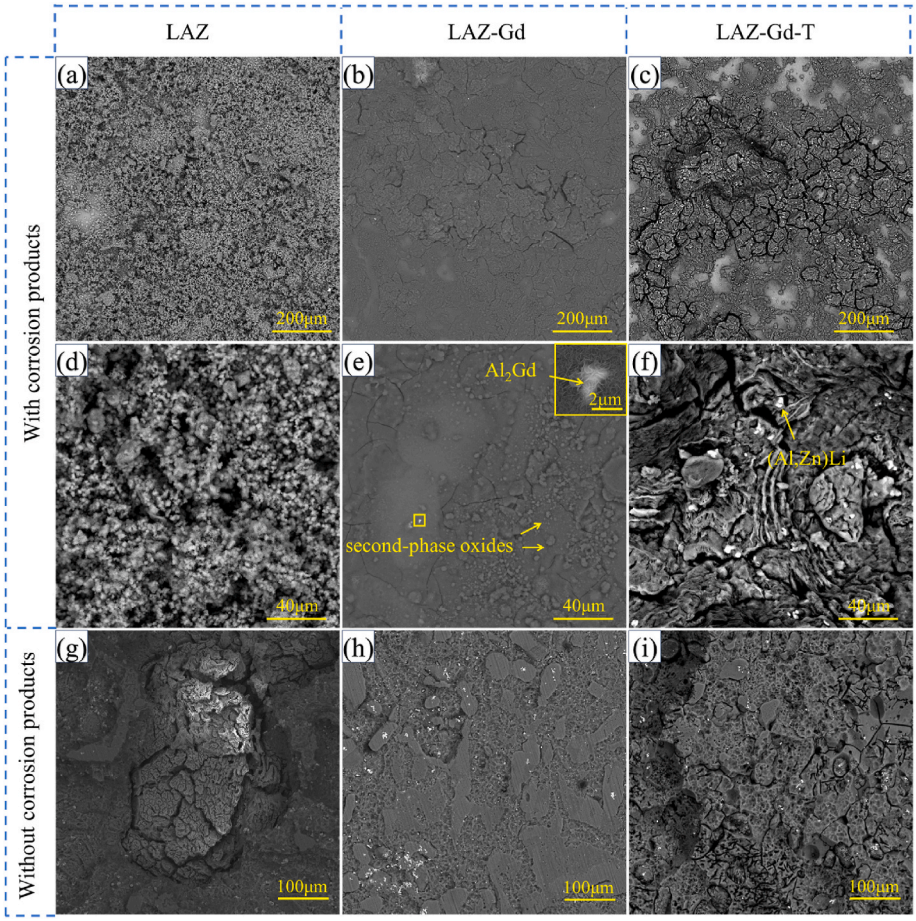

Fig. 12. Corrosion morphologies of the studied alloys after immersion in 3 *wt%* NaCl solution for 9 days: (a, d, g) LAZ; (b, e, h) LAZ-Gd; (c, f, i) LAZ-Gd-T.

and some corrosion pits began to form. Extending the immersion time to 24 h resulted in the appearance of even more corrosion pits. After 216 h of immersion, the LAZ alloy was severely corroded, with more than half of its surface covered by cloud-like corrosion products. Beneath these products, noticeably larger corrosion pits (compared with those observed after 24 h' immersion) were evident.

The corrosion morphologies of the studied alloys, after 9 days' immersion in the 3 *wt*% solution, were further examined using SEM, and the results are presented in Fig. 12, which includes images captured both with and without the corrosion products. Fig. 12(a–f) exhibits surface morphologies with corrosion products. An uneven and spongy corrosion films were observed on the LAZ alloy surface, suggesting its dissolution in the corrosion process. Such porous corrosion films cannot effectively inhibit the direct contact of the corrosion medium with the substrate, therefore, corrosion progress continuously, rationalizing the linear hydrogen evolution behavior observed in Fig. 10.

In contrast, the corrosion film formed on the LAZ-Gd alloy displayed different morphologies, featuring preferential cracks along the grain boundaries (Fig. 12(b)). Apparent mud cracks could be observed in the images captured at higher magnification (Fig. 12(e)), suggesting these areas had been severely corroded. Even after 216 h of immersion, some regions still remained intact, unaffected by the corrosion propagation. The LAZ-Gd-T alloy exhibited more pronounced mud-crack morphologies, with both the width and depth of the cracks exceeding those observed in the LAZ-Gd alloy. The regions that remained intact after corrosion were also markedly smaller compared with those in the LAZ-Gd alloy. These differences in corrosion morphology further indicate that the LAZ-Gd alloy experienced the least corrosion attack, which is consistent with the measured corrosion rates.

When the corrosion products were removed, the underlying corrosion footprint on the sample surface was revealed, as shown in Fig. 12 (g–i). Numerous corrosion pits with considerable diameter and depth were observed in the LAZ alloy, one of which is shown in Fig. 12(g). After removal of the corrosion film, the intact areas of the LAZ-Gd alloy became even more apparent. The corroded regions in the LAZ-Gd alloy were much shallower, and a large number of tiny corrosion pits were visible at the bottoms of these shallowly corroded areas. Moreover, the secondary-phase particles became exposed in Fig. 12(g) due to the dissolution of the surrounding β-Li matrix and α-Mg embeds. The corrosion pits in the LAZ-Gd-T alloy were larger than those in the LAZ-Gd alloy but smaller than those in the LAZ alloy, and a much lower fraction of secondary-phase particles remained on the corroded surface. Because the secondary phases generally possess a nobler corrosion potential than the matrix and embeds [41,42], they act as cathodic sites and are not consumed during corrosion. However, these particles can detach from the sample once the adjacent anodic regions are fully dissolved. The more severe corrosion experienced by the LAZ and LAZ-Gd-T alloys caused a greater number of detached particles to drop into the solution. Consequently, the fraction of secondary-phase particles remaining on these two samples after corrosion was much lower, even though the initial particle fraction prior to testing was higher in the LAZ alloy. It should be emphasized that the addition of Gd in the LAZ-Gd alloy promotes the formation of the Al_2Gd phase while suppressing the formation of the (Al,Zn)Li and $(Li,Mg)_3(Al,Zn)$ phases (as confirmed by the XRD results in Fig. 3). These changes in phase composition reduce the corrosion potential difference between the secondary phases and the surrounding microstructure, thereby mitigating localized galvanic corrosion. As a result, the corrosion behavior in the LAZ-Gd alloy transitions from pitting to a more uniform corrosion.

Cross-sectional corrosion morphologies of the different alloys after 9 days' immersion in the 3 *wt*% NaCl solution are shown in Fig. 13, where the corrosion films and their adhesion to the sample surfaces are more clearly revealed. Overall, the corrosion film on the LAZ alloy exhibits far greater unevenness than those on the other two alloys. Once corrosion pitting initiated in the LAZ alloy, a porous corrosion film began to form. This film could not effectively hinder the underlying corrosion, leading to the continuous deepening of the pitting and formation of additional corrosion products. Because corrosion of magnesium alloys is typically accompanied by volumetric expansion, these localized corrosion regions bulged outward from the sample surface (Fig. 13(a)).

In contrast, both Gd-containing alloys developed a significantly more uniform corrosion film. In the LAZ-Gd alloy, the intact α-Mg phases extending from the substrate into the corrosion layer appear to have temporarily hindered corrosion propagation. This initial protective effect is understandable, as the β-Li phase is known to be more corrosion-susceptible than α-Mg. Nonetheless, this inhibition is transient; owing to its intrinsic electrochemical activity in NaCl solution, the α-Mg phase itself eventually corrodes, as corroborated by the observed partial dissolution of some α-Mg embeds. Such observation indicated that the solution of Gd in the α-Mg may have increased its electrochemical stability, as no α-Mg inhibition on corrosion propagation had been observed in the LAZ alloy (Fig. 13(a)). Moreover, incorporation of

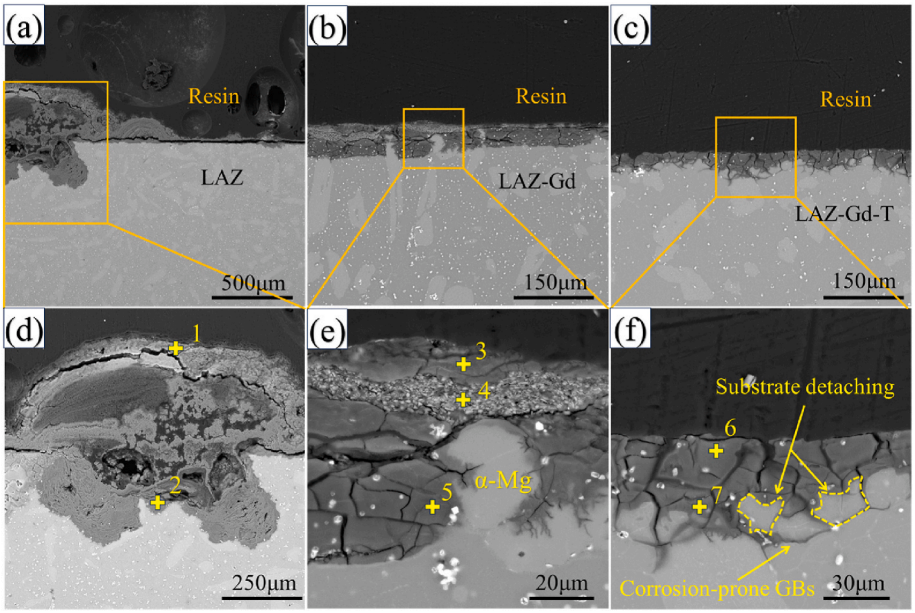

Fig. 13. Cross-sectional BSE images of (a, d) LAZ, (b, e) LAZ-Gd and (c, f) LAZ-Gd-T alloys after immersion in 3 wt % NaCl solution for 9 days.

secondary phase particles was detected in the corrosion films of the two Gd-containing alloys, while no such incorporation occurred in the corrosion film on the LAZ alloy. Furthermore, the chemical compositions across the film thickness were not uniform, and this heterogeneity was indicated by distinct contrast variations of the BSE images, particularly in the LAZ and LAZ-Gd alloys. The chemical compositions of various regions selected from the corrosion film were analyzed using EDS, and the results were summarized in Table 6. For the LAZ alloy, analyses were conducted on regions at the top (site #1) and bottom (site #2) of the corrosion pits. The top region consisted mainly of Mg and O (with trace Al); its Mg:O atomic ratio of around 0.6 closely matches the theoretical value for $Mg(OH)_2$ (0.5), but due to the inherent inability of EDS to detect ultra-light elements such as Li, this ratio should only be considered as a reference. Consequently, while the exact stoichiometry remains unconfirmed, the results still indicate that Mg-based hydroxide is likely a major corrosion product in this region. Similar chemical composition had been measured from the bottom site of the corrosion pit, appreciable amount of Zn had also been identified there. The atomic ratio of Mg:O is about 0.8 at site #2, which is close to that in MgO, suggesting that the corrosion products at the pit bottom may differ slightly from those at the top, possibly involving Mg-based oxide/hydroxide species. The difference between the outer and inner corrosion products observed here is also consistent with previous reports [34,43].

Three distinct morphologies could be observed from the cross-sectional BSE images of the LAZ-Gd alloy (Fig. 13(e)). The top (site #3) and bottom (site #5) regions exhibited similar features, consistent with the typical corrosion morphology of Mg alloys reported in the literature [34]. In contrast, the middle region (site #4) displayed a unique "gravel-paved" appearance. As summarized in Table 6, the chemical compositions of these regions were also distinct. Although the top and bottom regions shared a similar elemental profile (Mg, O, Al, and Zn), the concentrations of individual elements varied slightly between the two. The atomic ratio of Mg:O in the top and bottom regions were around 0.7 and 0.8, respectively. Therefore, similar phase compositions could be expected from the two regions. However, apart from the aforementioned elements, more concentrated Gd (as compared with its nominal concentration in the alloy (Table 1) had been detected in the middle region (#4). The Mg:O ratio in this region was only about 0.17, dramatically lower than that in MgO (1) or $Mg(OH)_2$ (0.5), implying that the excess oxygen was likely bonded with other elements such as Al, Zn, Gd, and also possibly Li. Indeed, the combined atomic concentration of $3n_{Al}+2n_{Mg} + 1.5n_{Gd} + n_{Zn}$ was very close to the measured oxygen content, suggesting that the middle region consisted of a mixture of $Al(OH)_3$, $Mg(OH)_2$, Gd_2O_3 and ZnO. It is also noteworthy that the cracks observed in other regions were absent in the middle region, resulting in a denser corrosion product layer that may have provided limited protective effect to the underlying substrate.

The chemical composition of the corrosion film formed on the LAZ-Gd-T alloy appeared uniform, as the two analyzed regions exhibited similar elemental profiles (Site #6 and #7). However, the presence of pronounced cracks suggests that this film did not serve as an effective barrier against further corrosion. Moreover, the compact "gravel-paved" region observed in the LAZ-Gd alloy was absent in the LAZ-Gd-T alloy, possibly due to the formation of quasi-continuous (Al,Zn)Li phase in the annealing treatment (Fig. 1). In the corrosion process, corrosion tends to penetrate along the quasi-continuous (Al, Zn)Li phases (Fig. 12). Once these penetrations interconnect, parts of the substrate become mechanically isolated and can detach/spall before being fully corroded. Examples of such undercut regions are highlighted by the dashed yellow lines in Fig. 12. This substrate detachment would repeatedly disrupt the possible deposition and retention of Gd-compounds, preventing the development of a stable Gd-enriched compact layer. The layered structure of corrosion film containing the compact region on the LAZ-Gd alloy is likely the main reason for its superior corrosion resistance compared with the other two alloys.

Table 6
EDS results collected from the points marked in Fig. 13 (*at.* %)

Elements	LAZ		LAZ-Gd			LAZ-Gd-T	
	1	2	3	4	5	6	7
O	61.5	53.8	55.4	73.9	54.0	50.5	49.1
Mg	38.3	45.3	39.9	12.4	43.9	39.8	41.9
Al	0.1	0.6	4.4	13.3	1.9	9.1	8.2
Gd	–	–	–	0.1	–	–	–
Zn	0.1	0.3	0.3	0.3	0.2	0.6	0.8

The surface chemistry of the samples after 9 days' immersion in 3 wt % NaCl solution was analyzed using XPS, and the corresponding results were displayed in Fig. 14. Generally, apparent Al*2s*, Mg*2p* and Zn*2p* signals had been identified, suggesting their presence on the superficial surface of the corroded alloys. No meaningful Gd 3*d* signal could be detected, likely due to its very low concentration on the sample surface, which results in a poor signal-to-noise ratio insufficient for reliable analysis. Indeed, the SEM-BSE image shown in Fig. 13 (e) confirms that Gd is mainly localized beneath the top surface layer, beyond the maximum depth accessible by XPS. One prominent peak was collected from the Al *2s* core level, at the binding energy (BE) of around 119 eV (Fig. 14(a)), suggesting the presence of compounds containing $Al(OH)_3$ [44] in the corrosion film. The intensity of the Al 2*s* peak in the LAZ alloy is significantly lower than that in the Gd-containing alloys, due to the lower Al concentration in the corrosion film formed on LAZ (as consistent with the EDS analysis shown in Table 6.

The characteristic binding energies of Li 1*s* and Mg 2*p* are very close, therefore, the corresponding spectra was collectively acquired in the binding energy range of 65-45 eV, as shown in Fig. 14(b). Among the three alloys, not any Li 1*s* peaks had been observed in their theoretical binding energy ranges of 60-52 eV, indicating the absence of Li on the superficial surface of the corroded alloys. Previous studies [44,45] also reported that XPS analysis of dual-phase Mg–Li alloys after long-term immersion corrosion revealed no detectable Li signal. The absence of reliable Li1*s* suggests that lithium compounds may exist deeper in the film, beyond the detection limit of XPS. Typical Mg 2*p* peaks centered around BE = 49.4 eV were observed. The Mg 2*p* peak can be deconvoluted into two sub-peaks, with BEs of 49.5 eV and 49.76 eV corresponding to Mg $2p_{3/2}$ and Mg $2p_{1/2}$, respectively. In the present measurement, the energy separation between these two components is approximately 0.26 eV, consistent with values reported in earlier studies [46]. The characteristic BE of Mg $2p_{3/2}$ (49.5 eV) indicates that Mg on the corroded surface exists predominantly in the form of $Mg(OH)_2$ [45]. Distinct peaks with binding energy difference of ΔBE = 23 eV can be observed form the Zn2*p* core-level spectra, corresponding to the orbital splitting of Zn$2p_{3/2}$ (BE = 1021.4 eV) and Zn$2p_{1/2}$ (BE = 1044.7 eV), respectively. Therefore, the Zn atoms in the corroded surface exists in the form of ZnO [47,48]. It should be noted that Zn Auger peaks were also observed in the Zn 2*p* spectra at BE = 1017 eV [49]. In addition, the O1*s* spectra can be deconvoluted into two components located at 531 eV and 533 eV. The peak at 531 eV is attributed to metal oxides [50], whereas the higher-BE component at 533 eV corresponds to hydroxides [46]. This further supports that the corrosion products on the surface mainly consist of $Mg(OH)_2$ together with a small amount of oxide species. The presence of $Al(OH)_3$, $Mg(OH)_2$ and ZnO indicated by the XPS analysis aligns well with the atomic ratio analysis based on Fig. 13 and Table 6.

Given the multilayer structure observed in the cross-sectional morphology of the corroded LAZ-Gd alloy, its corrosion film was further analyzed using TOF-SIMS depth profiling method, the mass spectra collected was shown in Fig. 15 to reveal the substances formed in the immersion process. The two most intense peaks in Fig. 15 correspond to mass-to-charge ratios of 1 and 12, which are attributed to H^- and C^-, respectively. Their high intensity arises mainly from the fact that hydrogen and carbon are ubiquitous surface species originating from adsorbed hydrocarbons, moisture, and residual gases in the analysis

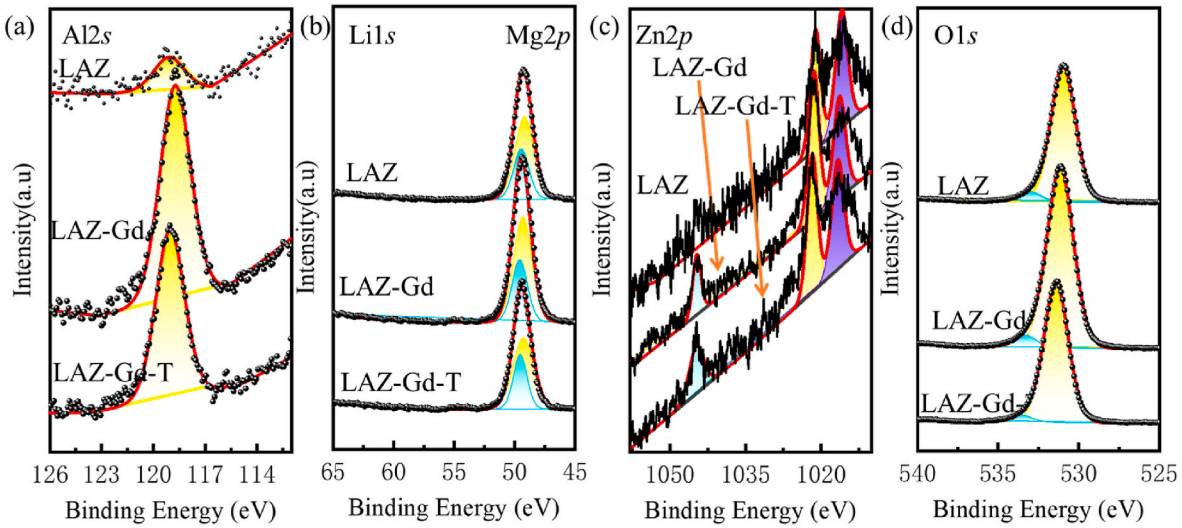

Fig. 14. XPS spectra collected from the corroded alloys after 9 days' immersion in the NaCl solution: (a) Al2*s*, (b) Mg2*p* and Li 1*s*; (c) Zn 2*p*; (d) Gd.

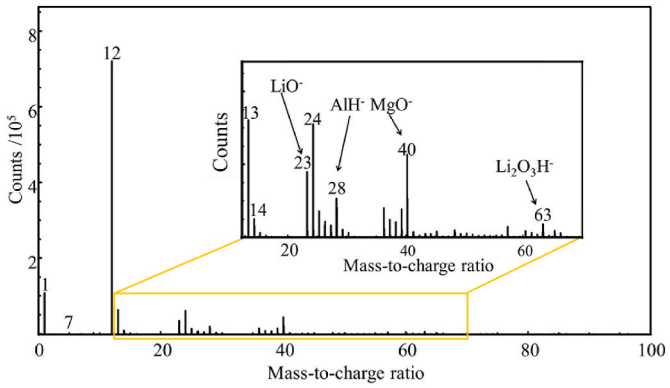

Fig. 15. Mss-to-charge ratio spectra of LAZ-Gd sample.

chamber, making them inherently abundant in the near-surface region during TOF-SIMS measurements. The mass spectral signals associated with the analyzed samples are mostly concentrated in the *m/z* range of 12-65, and a magnified view of this region is also presented in Fig. 15.

Four meaningful signals were identified at *m/z* 23, 28, 40, and 63, corresponding to the LiO^-, AlH^-, MgO^-, and $Li_2O_3H^-$ cluster ions, respectively. The LiO^- and $Li_2O_3H^-$ species represent different fragmentation or cluster-formation forms of LiOH, while AlH^- and MgO^- originate from the Al-containing intermetallic compound (Al-IMC) and $Mg(OH)_2$, respectively. The formation modes of these species are consistent with the typical $M_nH_m^-$, $M_nO_m^-$, $M_nO_mH^-$, and M_n^- cluster ions commonly observed in TOF-SIMS analyses [51]. Notably, signals beyond *m/z* 65 were also examined in the full mass spectrum. However, their intensities were significantly weaker compared to those within the 12-65 range and approached the background level, resulting in limited signal-to-noise ratios and insufficient reliability for meaningful spatial or depth-profile analysis. In contrast, the 12-65 *m/z* region exhibited the strongest and most information-rich signals, which are directly associated with the dominant light-element species constituting the corrosion film. Therefore, the discussion was focused on this range to ensure data clarity and analytical reliability.

The variation of the spectrum intensity of each species along with the etching time (i.e., from the sample surface toward the substrate) is shown in Fig. 16(a). Fig. 16(a) presents the depth profiles of four selected secondary ion signals: MgO^-, AlH^-, $Li_2O_3H^-$ and LiO^-. The

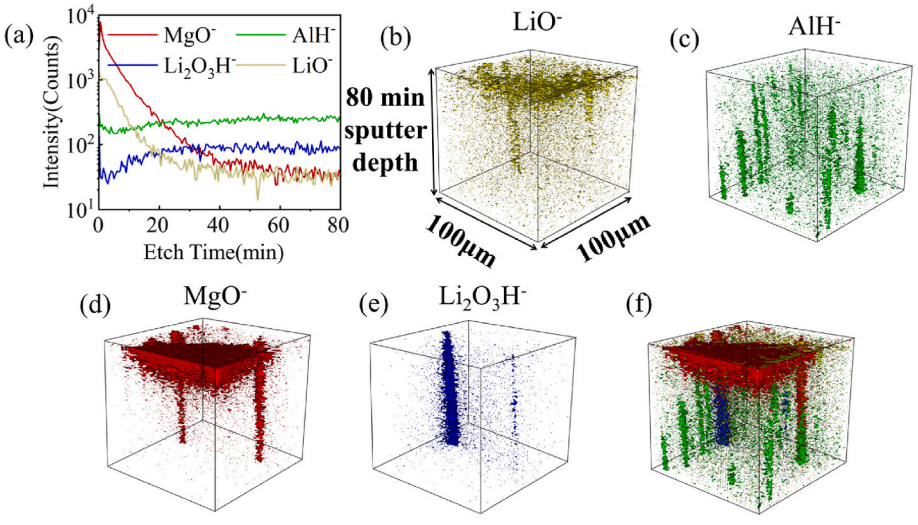

Fig. 16. (a) TOF-SIMS signal intensity variation along with the etching time, and the reconstructed 3D distribution of each species within the corroded film: (b) LiO^-, (c) AlH^-, (d) MgO^- (e) $Li_2O_3H^-$ and (f) the combined distribution of all species.

intensities of MgO^- and LiO^- gradually decrease with increasing etching depth, whereas the AlH^- and $Li_2O_3H^-$ signals remain nearly constant throughout the etching process. The decreasing trend of MgO^- and LiO^- are consistent with the inward progression of corrosion toward the substrate, further confirming that MgO^- and LiO^- originate from Mg $(OH)_2$ and LiOH, respectively.

The 3D spatial distribution of each substance identified in Fig. 15 was reconstructed as shown in Fig. 16(b–e). It is worth noting that, due to the microstructural heterogeneity of the film, the sputtering rate varied locally, making it impractical to establish a reliable depth (i.e., distance from the original surface) for the spectroscopic data. Therefore, the vertical axis in the 3D distribution map is presented as etching time rather than absolute depth. Similar with that observed in the cross-sectional BSE analysis, Fig. 16(b–e) also reveal the complex multilayered structure of the formed corrosion film. Fig. 16 (b) and (d) show the distributions of LiOH (LiO^-) and $Mg(OH)_2$ (MgO^-), respectively. When these two images are combined, the spatial distributions of LiOH and Mg $(OH)_2$ are found to exhibit a high degree of overlap, as shown in Fig. 16 (f). This overlap indicates that galvanic corrosion occurred at these locations, including galvanic coupling between α-Mg and β-Li as well as between the matrix and the second-phase particles.

According to the $Mg(OH)_2$ distribution shown in Fig. 16 (d), the large $Mg(OH)_2$ accumulation at the corner has a size comparable to that of the α-Mg phase (observed in Fig. 1), indicating that the $Mg(OH)_2$ originated from the corrosion of the α-Mg phase. In contrast, the two slim but deep $Mg(OH)_2$-rich regions coincides well with that of the LiO^- and $Li_2O_3H^-$ (LiOH) distributions, suggesting that it was formed by the corrosion of Mg dissolved in the β-Li matrix. As shown in Fig. 16(c) and (d), the spatial distributions of Al-IMC and LiOH exhibit a similar cylindrical morphology. It is also noted that the overlapped ion map in Fig. 16 (f) reveals a complementary relationship between the Al-IMC distribution and the LiOH distribution shown in Fig. 16 (e). This complementary pattern indicates that the LiOH observed in Fig. 16 (b) originates from galvanic corrosion occurring between the β-Li matrix and the second-phase particles (the concentration of Al in the secondary phases had been proven by Table 2). By comparing the penetration depths of the different species, it can be inferred that the galvanic attack at the second phase/matrix interface extends much deeper (as compared with the dissolution of β-Li matrix due to its potential difference with its adjacent α-Mg embeds). This indicates that galvanic coupling involving the second-phase particles is more intense and contributes more significantly to the inward propagation of corrosion.

Fig. 17 schematically illustrates the corrosion mechanisms of the studied alloys, along with detailed views of the local corrosion morphologies at the interfaces between the β-Li, α-Mg and second-phase particles. For the LAZ alloy, the presence of (Al,Zn)Li and $(Li,Mg)_3(Al,Zn)$ phases induce micro-galvanic corrosion between the matrix and these secondary phases. In this process, the (Al,Zn)Li and $(Li,Mg)_3(Al,Zn)$ phase acts as the cathode, while the matrix (α-Mg and β-Li) serves as the anode, leading to anodic dissolution of the matrix surrounding the (Al,Zn)Li particles. Once the matrix is corroded and the internal (Al,Zn)Li particles are exposed, corrosion pits further enlarge under the effect of galvanic corrosion, as shown in Fig. 17 (a) (such hypothesis had been indicated by the cross-sectional images shown in Fig. 13). With the addition of Gd, some Al-containing secondary phases are replaced by Al_2Gd compound, significantly reducing the galvanic effect. As a result, the LAZ-Gd alloy exhibits much shallower corrosion pits under the same immersion conditions. In the LAZ-Gd-T alloy, annealing treatment causes the secondary phases to partially dissolve back into the matrix and subsequently reprecipitate as finer $(Li,Mg)_3(Al,Zn)$ particles along with larger (Al,Zn)Li phases. The finely dispersed $(Li,Mg)_3(Al,Zn)$ particles generate smaller and more uniformly distributed corrosion pits through micro-galvanic interaction with the matrix. In addition, the larger (Al,Zn)Li particles have a reduced contact area with the matrix, further mitigating galvanic corrosion. This explains the reduced charge transfer resistance (R_t) in the LAZ-Gd alloy other than in the LAZ-Gd-T alloy in electrochemical impedance spectroscopy. However, the oxide film formed on the LAZ-Gd alloy after corrosion provides better protection, resulting in slightly better corrosion resistance compared to the LAZ-Gd-T alloy.

4. Conclusion

This study systematically investigated the effects of partial Zn substitution by Gd (LAZ-Gd) and subsequent annealing treatment (LAZ-Gd-T) on the microstructure and corrosion behavior of a dual-phase Mg–Li alloy containing Al and Zn (LAZ alloy). The main findings are summarized as follows.

(1) All alloys exhibit dual-phase α-Mg and β-Li microstructures with various secondary phases. In the LAZ alloy, (Al,Zn)Li and $(Li,Mg)_3(Al,Zn)$ are present, whereas the LAZ-Gd alloy additionally contains Al_2Gd, accompanied by reduced fractions of (Al,Zn)Li and $(Li,Mg)_3(Al,Zn)$. Annealing treatment did not alter the secondary phase compositions but refined their sizes in the LAZ-Gd-T alloy.

(2) EIS analysis indicates that Gd addition significantly increases the charge transfer resistance of the LAZ alloy, which is further enhanced by annealing, suggesting that both Gd addition and annealing reduce corrosion susceptibility.

(3) The corrosion film plays a critical role in governing the corrosion performance. On the LAZ alloy, the film primarily consists of porous $Mg(OH)_2$ and $Al(OH)_3$. In contrast, the LAZ-Gd alloy develops an additional compact layer enriched with Gd-containing compounds, which effectively suppresses corrosion propagation. However, this compact layer is absent on the LAZ-Gd-T surface. As a result, the LAZ-Gd alloy exhibits the most superior corrosion resistance among the studied materials.

(4) This study demonstrates a pathway to develop Mg–Li alloys with reduced density and enhanced corrosion resistance. The density

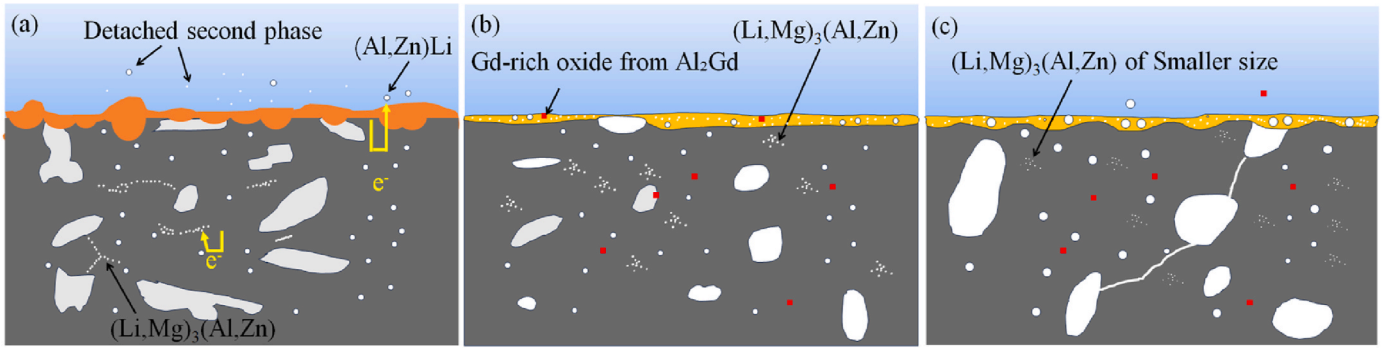

Fig. 17. Corrosion mechanism for (a)LAZ, (b)LAZ-Gd and (c)LAZ-Gd-T alloys.

reduced from 1.52 g/cm^3 (LAZ) to 1.50 g/cm^3 (LAZ-Gd), while the corrosion rate significantly reduced from 2.55 mm/y to 0.63 mm/y (LAZ-Gd) and 1.29 mm/y (LAZ-Gd-T).

Declaration of competing interest

The authors declare that they have no known competing financial interests or personal relationships that could have appeared to influence the work reported in this paper.

Acknowledgment

This work is supported by the Natural Science Foundation of Hunan Province (Grant No. 2023JJ30673) and the Central Guidance for Local Science and Technology Development Funds Project of Henan Province (Grant No. Z20231811076); Gang Zeng appreciates the support from The Science and Technology Innovation Program of Hunan Province (Grant No. 2022RC1081) and the National Defense Basic Research Program (Grant No. JCKY2023204A005).

References

[1] Ma X-c, Jin S-y, Wu R-z, Wang J-x, Wang G-x, Krit B, Betsofen S. Corrosion behavior of Mg−Li alloys: a review. Trans Nonferrous Met Soc China 2021;31:3228–54.
[2] Li J, Jin L, Wang F, Dong S, Dong J. Effect of phase morphology on microscopic deformation behavior of Mg–Li–Gd dual-phase alloys. Mater Sci Eng, A 2021;809:140871.
[3] Chang T-C, Wang J-Y, Chu C-L, Lee S. Mechanical properties and microstructures of various Mg–Li alloys. Mater Lett 2006;60:3272–6.
[4] Lin H, Deng B, Yan C, Wang S, Wang N, Li C. Effect of electrochemical cathodic hydrogen charging on the surface film of an ultralight Mg–Li–Zn alloy. Int J Hydrogen Energy 2025;159:150628.
[5] Zhu J, Lin Y, Li C, Wang N, Shi B, Zhang Z. Predicting mechanical properties of as-rolled eutectic Mg-8Li alloy via machine learning. J Mater Sci Technol 2026;254:45–60.
[6] Xu W, Birbilis N, Sha G, Wang Y, Daniels JE, Xiao Y, Ferry M. A high-specific-strength and corrosion-resistant magnesium alloy. Nat Mater 2015;14:1229–35.
[7] Kral MV, Muddle BC, Nie JF. Crystallography of the bcc/hcp transformation in a Mg–8Li alloy. Mater Sci Eng, A 2007;460–461:227–32.
[8] Li C, Liang D, Lin Y, Dong Y, Shi B, Yan C, Zhang Z. Effect of Li content on the surface film formed on the binary Mg–Li alloys in NaCl solution. Met Mater Int 2024;30:127–42.
[9] Zeng Z, Zhou M, Esmaily M, Zhu Y, Choudhary S, Griffith JC, Ma J, Hora Y, Chen Y, Gullino A, Shi Q, Fujii H, Birbilis N. Corrosion resistant and high-strength dual-phase Mg-Li-Al-Zn alloy by friction stir processing. Commun Mater 2022;3:18.
[10] Peng X, Liu W, Wu G, Ji H, Ding W. Plastic deformation and heat treatment of Mg-Li alloys: a review. J Mater Sci Technol 2022;99:193–206.
[11] Li C, Deng B, Dong L, Liu X, Du K, Shi B, Dong Y, Peng F, Zhang Z. Effect of Zn addition on the microstructure and mechanical properties of as-cast BCC Mg-11Li based alloys. J Alloys Compd 2022;895:162718.
[12] Li C, He Y, Huang H. Effect of lithium content on the mechanical and corrosion behaviors of HCP binary Mg–Li alloys. J Magnesium Alloys 2021;9:569–80.
[13] Zhou WR, Zheng YF, Leeflang MA, Zhou J. Mechanical property, biocorrosion and in vitro biocompatibility evaluations of Mg–Li–(Al)–(RE) alloys for future cardiovascular stent application. Acta Biomater 2013;9:8488–98.
[14] Liang X-l, Peng X, Ji H, Liu W-c, Wu G-h, Ding W-j. Microstructure and mechanical properties of as-cast and solid solution treated Mg−8Li−xAl−yZn alloys. Trans Nonferrous Met Soc China 2021;31:925–38.
[15] Pugazhendhi BS, Kar A, Sinnaeruvadi K, Suwas S. Effect of aluminium on microstructure, mechanical property and texture evolution of dual phase Mg-8Li alloy in different processing conditions. Arch Civ Mech Eng 2018;18:1332–44.
[16] Lin H, Ke X, Xiong G, Shi B, Zhang Z, Li C. The effect of rare Earth Y on the microstructure and mechanical properties of an As-Cast body-centered cubic Mg-11Li-6Zn alloy. Metals 2025;15:321.
[17] Sun Y-h, Wang R-c, Peng C-q, Wang X-f. Effect of Gd on microstructure, mechanical properties, and corrosion behavior of as-homogenized Mg−8Li−3Al−2Zn−0.2Zr alloy. Trans Nonferrous Met Soc China 2022;32:2494–509.
[18] Heng Z, Huang L, Zhang Q, Shi X, Shen J. Simultaneously improved strength and ductility in a Ce-doped dual-phase Mg–9Li alloy. J Mater Res Technol 2025;34:2501–11.
[19] Zhang C, Wu L, Zhao Z, Huang G, Jiang B, Atrens A, Pan F. Effect of Al on the microstructure, corrosion behavior and mechanical properties of Mg-4Li. Anti-corrosion Methods & Mater 2020;67:31–7.
[20] Li C, Deng B, Dong L, Shi B, Dong Y, Peng F, Zhang Z. Effect of Zn addition on the corrosion behaviours of as-cast BCC Mg-11Li based alloys in NaCl solution. Mater Des 2022;221:111019.
[21] Deng B, Liang D, Li C, Yan C, Dong Y, Wang N, Zhang Z, Han E-H. Effect of Zn addition on the stress corrosion cracking of as-cast BCC Mg-11Li based alloys. Corros Sci 2024;227:111707.
[22] He Y, Peng C, Feng Y, Wang R, Zhong J. Effects of alloying elements on the microstructure and corrosion behavior of Mg–Li–Al–Y alloys. J Alloys Compd 2020;834:154344.
[23] Manivannan S, Dinesh P, Mahemaa R, MariyaPillai N, Kumaresh Babu SP, Sundarrajan S. Corrosion behavior of as-cast Mg–8Li–3Al+xCe alloy in 3.5wt% NaCl solution. Int J Min Met Mater 2016;23:1196–203.
[24] Tong Z, Li C, Liang D, Chen M, Dong Y, Bian D, Yan C, Han E-H. Improving the corrosion resistance of an ultra-lightweight BCC Mg-Li-Zn alloy via controlling the microstructure by heat treatment. J Magnesium Alloys 2025;13:2325–42.
[25] Li C, Li X, Ke X, Dong Y, Wang N, Wang S, Zhang Z. Enhancing corrosion resistance of Mg-Li-Zn-Y-Mn alloy containing long period stacking ordered (LPSO) structure through homogenization treatment. Corros Sci 2024;228:111829.
[26] Li CQ, Liu X, Dong LJ, Shi BQ, Tang S, Dong Y, Zhang ZR. Simultaneously improved mechanical strength and corrosion resistance of Mg-Li-Al alloy by solid solution treatment. Mater Lett 2021;301:130305.
[27] Shi Z, Liu M, Atrens A. Measurement of the corrosion rate of magnesium alloys using Tafel extrapolation. Corros Sci 2010;52:579–88.
[28] Deng B, Lv S-H, Yang Q, Zhao D-Y, Fan J-Y, Qiu X. Lath-like phases formed at an extremely high temperature in a Mg–RE (RE = rare earth)–Al alloy. Rare Met 2024;43:3937–45.
[29] Fan J, Yang Q, Lv S, Meng F, Gu H, Zhang J, Cheng Y, Li R, Qiu X. Synergetic tensile properties and thermal conductivity of high-pressure die casting Mg-Al-RE alloys controlling by various Al and La additions. J Alloys Compd 2025;1032:181121.
[30] Ji H, Wu G, Liu W, Zhang X, Zhang L, Wang M. Origin of the age-hardening and age-softening response in Mg-Li-Zn based alloys. Acta Mater 2022;226:117673.
[31] Huang Y, Qi F, Sun J, Xu Y, Guo Y, Yu J, Yi L, Tao X, Wu G, Liu W. Strengthening dual-phase Mg-Li alloy through precipitation control. Mater Res Lett 2025;13:17–23.
[32] McAlister AJ. The al−li (Aluminum−Lithium) system. Bulletin of Alloy Phase Diagrams 1982;3:177–83.
[33] Zhang K, Wang C, Wang D-W, Li M-X, Ma Y-L, Hua Z-M, Zhang L-Y, Li J, Wang H-Y. Effects of solute redistribution during heat treatment on micro-galvanic corrosion behavior of dilute Mg-Al-Ca-Mn alloy. Corros Sci 2023;213:110971.
[34] Yin J, Li M, Yi F, Zhao X, Guan D, Wang K, Gao Y, Liu C. Effects of micro-alloying Ag on microstructure, mechanical properties and corrosion behavior of extruded Mg-2Zn-0.2Ca-xAg alloys. J Alloys Compd 2024;989:174376.
[35] Li CQ, Xu DK, Chen XB, Wang BJ, Wu RZ, Han EH, Birbilis N. Composition and microstructure dependent corrosion behaviour of Mg-Li alloys. Electrochim Acta 2018;260:55–64.
[36] Huang YS, Zeng XT, Hu XF, Liu FM. Corrosion resistance properties of electroless nickel composite coatings. Electrochim Acta 2004;49:4313–9.
[37] Song Y, Shan D, Chen R, Han E-H. Corrosion characterization of Mg–8Li alloy in NaCl solution. Corros Sci 2009;51:1087–94.
[38] Gao Y, Yerokhin A, Matthews A. Effect of current mode on PEO treatment of magnesium in Ca- and P-containing electrolyte and resulting coatings. Appl Surf Sci 2014;316:558–67.
[39] He Y, Zhang J, Li Z, Sun B, Wang L, Dong H, Yang Q, Liu S, Wu R, Zhang X, Qiu X. Insight into dissolution rate-regulated advanced films on Mg-Gd-Sm alloy with high anti-corrosion and discharge properties. Acta Mater 2025;290:120952.
[40] Gao Y, Yerokhin A, Parfenov E, Matthews A. Application of voltage pulse transient analysis during plasma electrolytic oxidation for assessment of characteristics and corrosion behaviour of Ca- and P-containing coatings on magnesium. Electrochim Acta 2014;149:218–30.
[41] Hu Z, Yin Z, Yin Z, Wang K, Liu Q, Sun P, Yan H, Song H, Luo C, Guan H, Luc C. Corrosion behavior characterization of as extruded Mg-8Li-3Al alloy with minor alloying elements (Gd, Sn and Cu) by scanning Kelvin probe force microscopy. Corros Sci 2020;176:108923.
[42] Peng X, Sun J-w, Liu H-j, Wu G-h, Liu W-c. Microstructure and corrosion behavior of as-homogenized and as-extruded Mg−xLi−3Al−2Zn−0.5Y alloys (x=4, 8, 12). Trans Nonferrous Met Soc China 2022;32:134–46.
[43] Fu Y-H, Chu P-W. Localized corrosion behavior and surface corrosion film microstructure of a commercial dual-phase LZ91 Mg alloy. npj Mater Degrad 2025;9:19.
[44] Sun Y, Zhang F, Wang R, Peng C, Ren J, Song G. Improving the corrosion resistance of Mg-8Li-3Al-2Zn alloy by combining Gd alloying and hot extrusion. J Alloys Compd 2023;964:171205.
[45] Sun Y, Wang R, Peng C, Cai Z. Microstructure and corrosion behavior of as-extruded Mg-xLi-3Al-2Zn-0.2Zr alloys (x = 5, 8, 11 wt.%). Corros Sci 2020;167:108487.
[46] Sebastian A Skaanvik, Henderson Jeffrey D, Noël James J, Biesinger Mark C. Speciation of magnesium surfaces by X-Ray photoelectron spectroscopy (XPS). Surf Interface Anal 2025;57:717–28.
[47] Nefedov VI, Salyn YV, Leonhardt G, Scheibe R. A comparison of different spectrometers and charge corrections used in X-ray photoelectron spectroscopy. J Electron Spectrosc Relat Phenom 1977;10:121–4.
[48] Strohmeier BR. Zinc aluminate (ZnAl2O4) by XPS. Surf Sci Spectra 1994;3:128–34.

[49] Antonides E, Janse EC, Sawatzky GA. LMM Auger spectra of Cu, Zn, Ga, and Ge. I. Transition probabilities, term splittings, and effective Coulomb interaction. Phys Rev B 1977;15:1669–79.
[50] Frankcombe TJ, Liu Y. Interpretation of oxygen 1s X-ray photoelectron spectroscopy of ZnO. Chem Mater 2023;35:5468–74.
[51] Ekar J, Panjan P, Drev S, Kovač J. ToF-SIMS depth profiling of metal, metal oxide, and alloy multilayers in atmospheres of H2, C2H2, CO, and O2. J Am Soc Mass Spectrom 2022;33:31–44.